Hysteresis with Quantum Dots in Micropillar Cavities

THESIS

submitted in partial fulfillment of the
requirements for the degree of

MASTER OF SCIENCE
in
PHYSICS

Author :	Thomas Ruytenberg, BSc
Student ID :	s1061488
Supervisors :	Morten P. Bakker, MSc
	Dr. Martin P. van Exter
2^{nd} corrector :	Prof.dr. Jan M. van Ruitenbeek

Leiden, The Netherlands, November 7, 2014

Hysteresis with Quantum Dots in Micropillar Cavities

Thomas Ruytenberg, BSc

Huygens-Kamerlingh Onnes Laboratory, Leiden University
P.O. Box 9500, 2300 RA Leiden, The Netherlands

November 7, 2014

Abstract

A cavity quantum electrodynamics system with quantum dots in micropillar cavities is studied. For resonant spectroscopy scans with high power ($\sim$1 nW), scanning hysteresis is observed in this system. This hysteresis is only present on the red side of the cavity resonance and exhibits a strong power dependence. A two-laser experiment is presented, which shows an intracavity field dependent blue-shift of the quantum dot frequency. Simulations show that this blue-shift causes the observed hysteresis. We propose accumulating charges around the oxide aperture in the micropillar as a cause for the blue-shift, by means of the quantum confined Stark effect. In a time resolved experiment, a millisecond timescale for the build-up time of this charging is obtained. We conclude with a future outlook, where we discuss a photon correlation and an interferometric experiment for which first steps have been taken.

Contents

Chapter 1

Introduction

In the search for more computing power, quantum information and quantum computing have become an active field of research. A quantum computer will be able to solve certain problems much quicker than a normal classical computer, making it an interesting research topic.

Building a quantum computer requires quantum bits (qubits). For these qubits, many systems have been proposed such as superconducting circuits [1], Rydberg atoms [2], defect centers like nitrogen vacancy centers in diamond [3] or phosphorus atoms in silicon [4], and quantum dots [5].

In this thesis, a system with quantum dots is studied. Quantum dots are also called artificial atoms, and are integrated in a solid-state environment. This way experiments on quantum dots are more easily performed than with single atoms, which require atom traps. These quantum dots can be optically controlled and in order to increase the light-matter interaction with the quantum dots, they are placed inside a microcavity. Such a cavity quantum electrodynamics (cavity QED) system, is not only interesting for quantum information schemes [6], but also for single photon switches [7] and generation of non-classical states of light [8, 9].

The structure of this master thesis is as follows:

The very basics of a cavity QED system are explained in Ch. 2. In Ch. 3, the sample structure and the general setup used for the experiments in this thesis are presented and explained. Chapter 4 contains the experimental observations on scanning hysteresis. These observations lead to a model which can reproduce the observed hysteresis. Finally, in Ch. 5 first steps

towards new experiments with this system are shown. Photon correlations in the system are measured which show intriguing features and an interferometric measurement technique is shown with first results.

Chapter 2

Theory

2.1 Dipole in a cavity

A cavity QED system consists of a dipole inside a cavity. The coupling between the dipole and the optical intracavity field alters the reflected and transmitted optical field and such a system is depicted in Fig. 2.1. To calculate the reflection and transmission intensities, the system is described in a quantum description by Heisenberg operator equations [10, 11].

$$\begin{aligned} \frac{d\hat{b}}{dt} &= -(i\omega_0 + \kappa_m + \kappa_s/2)\hat{b} + \sqrt{\kappa_m}(\hat{a}_{in} + \hat{c}_{in}) - ig\sigma_- \\ \frac{d\sigma_-}{dt} &= -(i(\omega_0 + \delta) + \frac{1}{2\tau})\sigma_- + ig\sigma_z\hat{b} \end{aligned} \tag{2.1}$$

$\hat{b}$ describes the intracavity field, ω_0 is the angular frequency of the cavity resonance, κ_m and $\kappa_s/2$ are the mirror and absorption amplitude loss rates, $\hat{a}$ and $\hat{c}$ the in- and output fields, g the vacuum Rabi frequency of the dipole, σ_- a dipole operator, δ the detuning between the dipole and the cavity, and $1/2\tau$ the decay rate of the dipole operator.

Using the input/output relations for the system, obtained by the boundary conditions for the fields at the mirrors,

$$\begin{aligned} \hat{a}_{out} + \hat{a}_{in} &= \sqrt{\kappa_m}\hat{b} \\ \hat{c}_{out} + \hat{c}_{in} &= \sqrt{\kappa_m}\hat{b} \end{aligned} \tag{2.2}$$

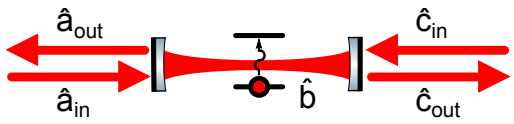

Figure 2.1: *The cavity QED system; a dipole in a cavity.*

and under the conditions of weak excitation and monochromatic input fields, such that $\sigma_z = -1$, these coupled equations can be solved for $\hat{c}_{out}$. Using single-sided injection at input channel $\hat{a}_{in}$ gives

$$\hat{c}_{out} = \frac{\kappa_m \hat{a}_{in}}{-i\Delta\omega + \kappa_m + \kappa_s/2 + \frac{g^2}{-i(\Delta\omega - \delta) + 1/2\tau}} \tag{2.3}$$

where $\Delta\omega$ is the laser angular frequency detuning with respect to the cavity. This can be rewritten to a more elegant equation in the following way [12]. We use $\kappa/2 \equiv \kappa_m + \kappa_s/2$ for the roundtrip amplitude loss and $\gamma_\perp \equiv 1/2\tau$ for the decay rate of the dipole operator or dephasing rate. Furthermore we introduce $\Delta \equiv 2\Delta\omega/\kappa$ as normalized laser-cavity detuning and $\Delta' \equiv (\Delta\omega - \delta)/\gamma_\perp$ as normalized laser-dipole system detuning

$$\hat{c}_{out} = \frac{\kappa_m \hat{a}_{in}}{-i\Delta\kappa/2 + \kappa/2 + \frac{g^2}{\gamma_\perp(1 - i\Delta')}} \tag{2.4}$$

We set $\eta_{out} \equiv 2\kappa_m/\kappa$ as output coupling efficiency and $C \equiv g^2/\kappa\gamma_\perp$ as the dimensionless cooperativity parameter. Together with $\hat{c}_{out} = t(\omega)\hat{a}_{in}$ we obtain an expression for the complex transmission

$$t(\omega) = \frac{\eta_{out}}{1 - i\Delta + \frac{2C}{1 - i\Delta'}} \tag{2.5}$$

The absolute transmission and reflection intensities can be obtained by

$$\begin{aligned} T(\omega) &= |t(\omega)|^2 \\ R(\omega) &= |1 - t(\omega)|^2 \end{aligned} \tag{2.6}$$

2.2 Quantum dots

In this work, quantum dots act as dipole in the cavity. Quantum dots are semiconductor nanostructures in which the electronic wavefunction is spatially confined in all three dimensions. Due to this confinement, the quantum dot can be approximated by the 'particle in a box' problem in quantum mechanics where the quantum dot is the box, and the particle is an electron or a hole. Because of this confinement, discrete atom-like energy states emerge. Therefore, a quantum dot can be seen as an artificial atom.

In the case of GaAs/InAs quantum dots, which are used in this study, a few monolayers of InAs are deposited onto GaAs by molecular beam epitaxy (MBE). Due to a 7% difference in lattice constants for GaAs and InAs, small islands of InAs are formed (Stranski–Krastanov growth mode). When capped of with GaAs, these InAs islands are confined by GaAs. This is shown in Fig. 2.2. Due to the fact of InAs having a lower electronic bandgap than GaAs, an electronic potential well is created, thereby confining the electronic wavefunction and forming quantum dots. By creating an n and p-doped layer around the quantum dot, the Fermi level can be tuned by applying an electric field. This way an electron can be tuned into the quantum dot in order to work with negatively charged quantum dots. Also the quantum confined Stark effect can be used to frequency tune a quantum dot. The electronic bandstructure created this way, is shown in Fig. 2.3 for both zero bias and forward bias.

The quantum dots can be optically excited. This can either be done resonantly, creating the electron-hole pair in the quantum dot, or off-resonantly. In the off-resonant case, an electron-hole pair is excited in either the InAs wetting layer, or the GaAs layer with a larger energy than the quantum dot ground state. This electron-hole pair can relax into the quantum dot due to its smaller bandgap, where it can recombine and emit a photon. This emission process is called photoluminescence.

Polarization selection rules are essential in describing the allowed transitions of the quantum dots. In Fig. 2.4 allowed optical transitions transitions are shown which are relevant for this work. For the exciton states, due to electron-hole interaction, a fine structure splitting of the two linear orthogonally polarized transitions is present. This is due to the fact that the manufactured quantum dots are not perfectly circular, but slightly elliptical in shape. For the trion states, a fine structure splitting is not present due to vanishing electron-hole interaction [13]. The two trion transitions

are right-hand and left-hand circularly polarized.

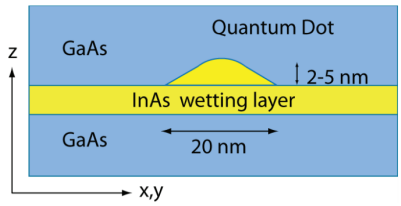

Figure 2.2: *A schematic view of a formed quantum dot, where the z direction is the growth direction*

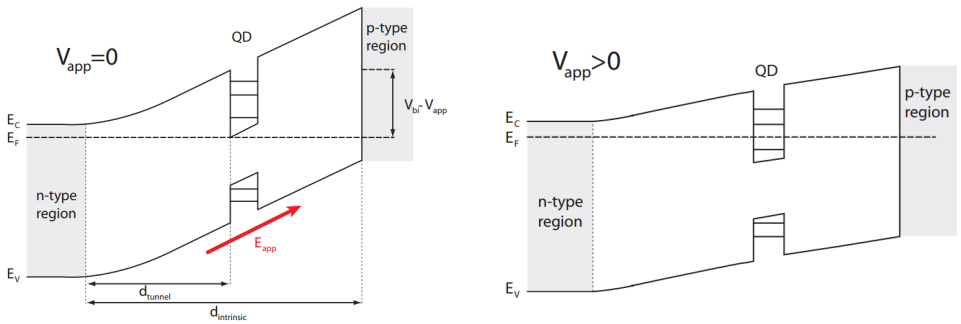

(a) (b)

Figure 2.3: *Bandstructure of a quantum dot with voltage control. By tuning the applied voltage, the Fermi level can be adjusted and the quantum dot can be charged. Also the quantum dot frequency is tuned this way via the quantum confined Stark effect. Based on Fig. 1.15 from Ref. [14]*

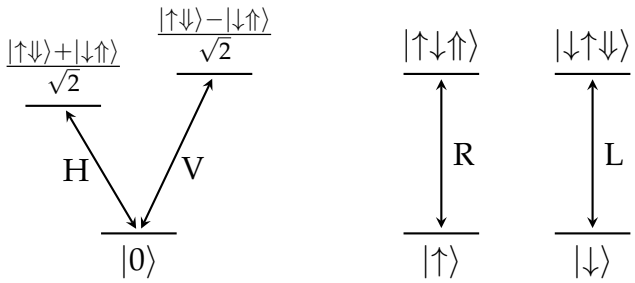

Figure 2.4: *Energy level diagram for both the exciton (left) and trion (right) transitions. The exciton transitions are linearly polarized, while the trion transitions are circularly polarized. For the exciton an energy splitting is visible, attributable to the fine structure. The vacuum state is denoted by $|0\rangle$ and $\uparrow/\downarrow$ ($\Uparrow/\Downarrow$) denote the electron (hole) up/down spin, defined in the growth direction of the quantum dot.*

Chapter 3

Setup

For the experiments described in Ch. 4, the setup depicted in Fig. 3.1 was used. In this chapter we will discuss this setup in detail.

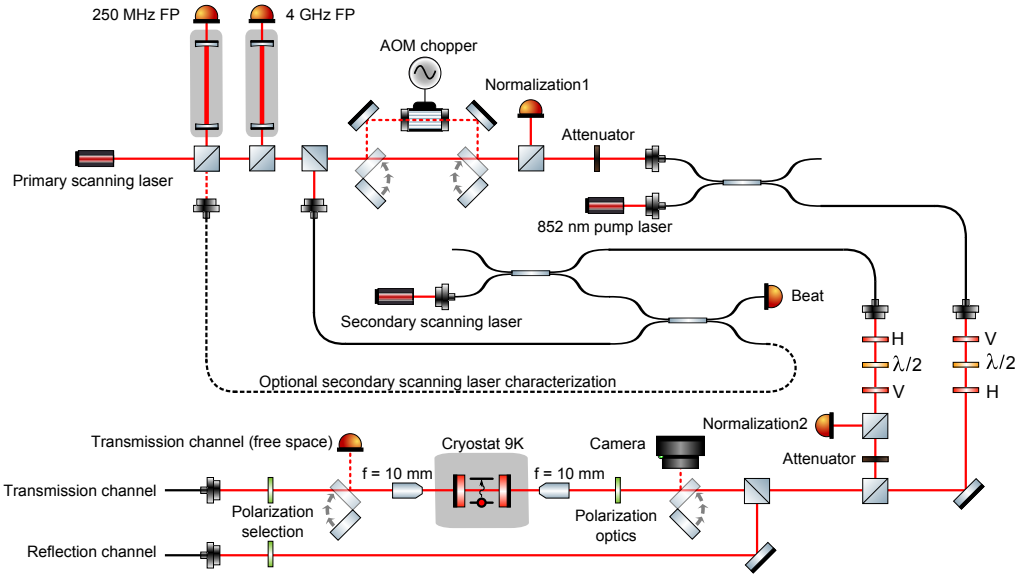

Figure 3.1: *Quantum dot spectroscopy setup.*

The primary scanning laser (New Focus, Velocity) can scan over a range of 70 GHz with a wavelength between 930 and 945 nm. This laser is first analyzed using two Fabry-Perot cavities to obtain a relative frequency scale.

It can then be modulated using an AOM if needed, after which it is coupled into a single-mode fiber-based beamsplitter together with an 850 nm pump laser. The pump laser can be used for alignment of the setup and PL measurements. A polarizer/half-waveplate/polarizer sequence is used to fine-tune the intensity and to set the polarization linear and horizontal with respect to the optical table. Before coupling into the sample, polarization optics can be used to select either one of the finesplit linear exciton transitions or one of the circular trion transitions (see Fig. 2.4). In both transmission and reflection, a polarization selection can be done using polarization optics after which the light is coupled into a fiber and can be detected by either a PDA100A Thorlabs Si amplified photodetector (range: $> 1\,\mu W$), a Model 2151 New Focus Visible FemtoWatt photoreceiver (range: 100 pW - 10 nW) or a SPCM-AQR-14-FL Perkin Elmer single photon counting module (SPCM) (range: < 10 pW without ND filters). All the mentioned power, are powers measured just before the front objective and are therefore the powers that are injected into the cavity QED system.

A second scanning laser (Toptica Photonics, DL pro) can be used. However, this laser does not have its own Fabry-Perot cavities to do frequency characterization during a scan. While not doing a scan with the primary scanning laser, the secondary scanning laser can temporarily be fed into the Fabry-Perot cavities for mode-hop tuning of the laser. By setting the polarization of the second laser orthogonal to the primary scanning laser, the second laser can be filtered out before collection in the transmission or reflection channel.

3.1 Cryostat

The quantum dot sample is cooled down to 9 Kelvin using a pulse tube cryostat system (Janis). The pulse tube itself is mechanically isolated from both the sample and the optical setup in order to prevent vibrations influencing optical alignment. Thermal contact between the pulse tube and the coldfinger to which the sample is mounted is achieved via a helium exchange gas. This does however restrict the minimum temperature of the sample to about 9 K before the helium starts condensing, which would then create mechanical contact. Pressure waves created by the pulse tube are absorbed by a flexible helium gas reservoir at atmospheric pressure. The sample is optically accessible via two viewing ports on both side of the sample allowing both reflection and transmission measurements.

3.2 Software

The setup is controlled using Python scripts which control a National Instruments digital acquisition card (DAQ) card. By applying a voltage ramp on the scanning laser frequency modulation input, the laser can be scanned over the cavity resonance. During a scan, the output voltages of photodiodes in the setup are recorded using the DAQ card. For a scan with only the primary scanning laser, the photodiodes named '250 MHz FP', '4 GHz FP', 'Normalization 1', and the reflection and transmission photodiodes are recorded. If for reflection and transmission SPCMs are being used, not output voltages are recorded, but a counter module of the DAQ card is used to record photon counts.

Using the transmission signal of the Fabry-Perot cavity during a scan, the applied voltage ramp to the frequency modulation input of the laser can be converted to a relative frequency scale using analysis scripts written in MATLAB.

3.3 Samples

Micropillar cavities with InAs/GaAs quantum dots, shown in Fig. 3.2 were used. These samples were grown using MBE at the University of California Santa Barbara (UCSB). Also additional cleanroom steps were performed at UCSB, such as trench etching, wet oxidation and metal contact deposition.

For out of plane confinement of the light in the quantum dot region, two distributed Bragg reflectors (DBR) are used (see Fig. 3.2(a)). For in-plane mode confinement of the light, an oxide aperture is applied by oxidizing an AlAs layer using a wet oxidation process. This reduces the refractive index, confining the light in-plane and resulting in a modal volume of $2.7\,\mu m^3$ and a quality factor of 2.7×10^4 The cavities have been made polarization degenerate up to 1 GHz by making the oxidation front elliptical, allowing full polarization control of the incoming light on the quantum dot [15].

Furthermore, n and p-doped layers are grown underneath and above the quantum dot layer to be able to use the quantum confined Stark effect. This way the quantum dot transitions can be tuned in resonance with the

cavity. Electrical contacts from the bulk sample to the n and p-doped layer in the micropillar are provided by the three bridges.

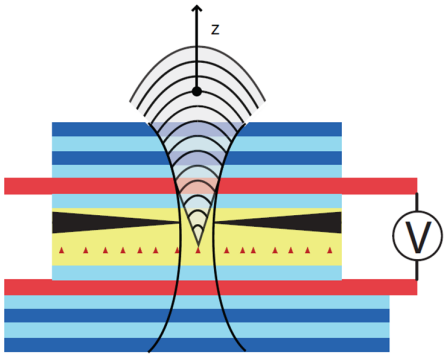

(a) Schematic view of the sample. Photoluminescence from the quantum dot is shown.

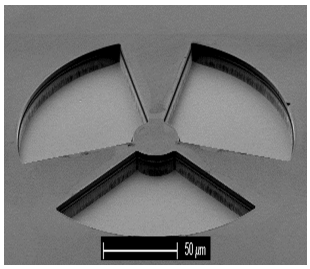

(b) SEM image of a micropillar sample. The micropillars used in this master thesis have a diameter of ∼30 µm.

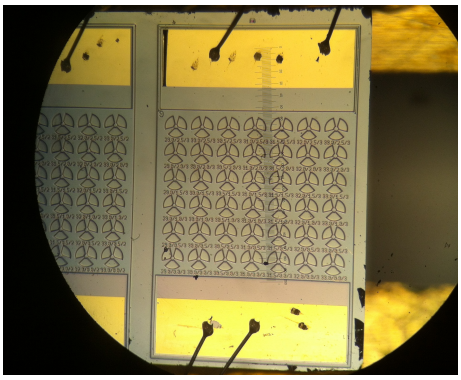

(c) Optical microscope image of a sample containing 42 cavities per array. The upper and lower voltage contacts are connected to the n and p-doped layers.

Figure 3.2: *The sample is a micropillar cavity consisting of two DBR mirrors with a layer of quantum dots in between. It contains an oxide aperture for in-plane mode confinement and doped layers for quantum confined Stark tuning of quantum dots into resonance with the cavity.*

Chapter 4

Experimental results

In this chapter, first some sample characteristics are shown and resonant spectroscopy scans at low power ($\sim$1 pW) are presented with theoretical fits. The rest of the chapter covers a hysteresis effect which appears at higher powers. Different experiments are performed in order to find the physical mechanism behind this hysteresis. Using the observations of these experiments, a physical mechanism is proposed and using a simple model, simulations are performed to reproduce the hysteresis.

4.1 Sample characteristics

Spatial scans of a sample for resonant and off-resonant probing of the reflection and transmission channel are presented in Fig. 4.1. These images were obtained by scanning the front objective in an x-y grid using a xyz piezo stage (Physik Instrumente), thereby moving the focus of the probe laser over the sample. A probe power $> 100\,\mu$W was used, far above the saturation power of the quantum dots, allowing for examination of the cavity properties only. For the resonant case ($\lambda_{laser} \approx \lambda_{cavity} = 940.48 \pm 0.02$ nm), a Gaussian transmitted beam profile is observed with a FWHM of 2.3 ± 0.3 µm. For the off-resonant case ($f_{laser} \approx f_{cavity} - 30$ GHz, with a FWHM of the cavity $\sim$15 GHz), more light is reflected from the cavity. The overall reflection and transmission collection efficiencies are 10% and 4% respectively, with respect to the power before the front objective. Figure 4.1(c) shows the reflection of the sample, just around the cavity. A non-uniform reflection background is observed. This non-uniformity was

first observed just after a full thermal cycle of the sample (9-273-9 K). All measurements in this thesis have been done under these conditions. After another thermal cycle, the non-uniformity disappeared, indicating that it might have been caused by condensed water or nitrogen.

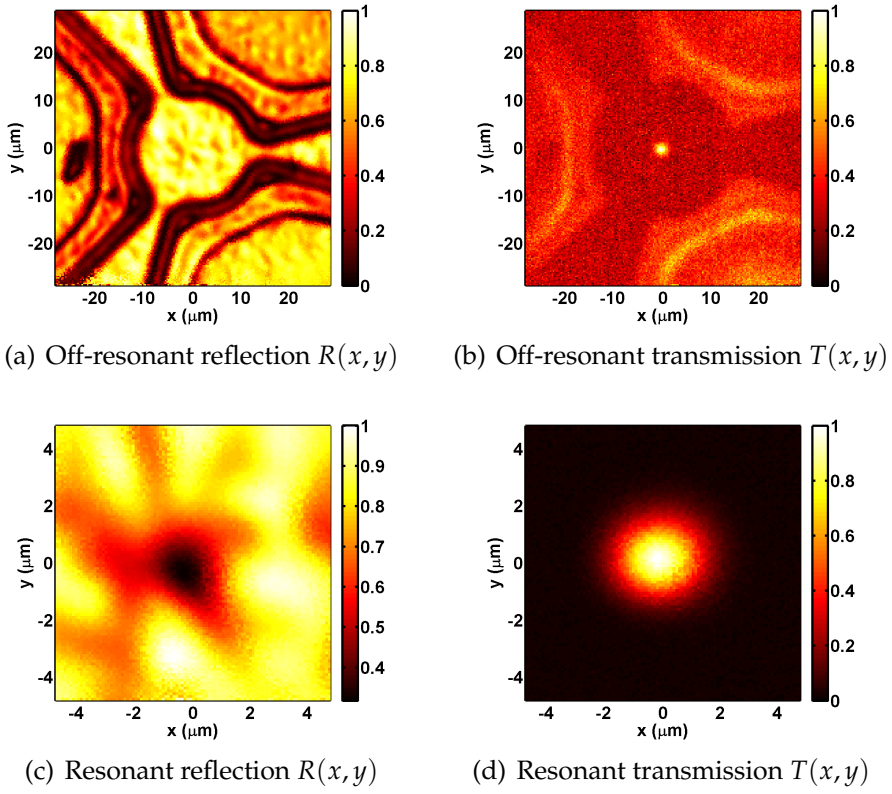

(a) Off-resonant reflection $R(x, y)$ (b) Off-resonant transmission $T(x, y)$

(c) Resonant reflection $R(x, y)$ (d) Resonant transmission $T(x, y)$

Figure 4.1: *Spatial scans of the micropillar cavity. The off-resonant scans are off-resonant by ∼30 GHz, with the FWHM of the cavity being ∼15 GHz. For all figures the cavity center is located at (0,0). The color scales are relative. In (b), a minor transmitted fraction is observed due to a higher amplification factor of the photodiode for this particular scan.*

When spatially aligned with the cavity, resonant reflection and transmission spectroscopy scans can be done. Figure 4.2 presents both reflection and transmission signal as a function of the scanning laser frequency. A quantum dot was tuned in resonance with the cavity by applying a bias voltage over the P-I-N junction. Fitting the obtained reflection curves with Eq. 2.5 and Eq. 2.6 results in the fit parameters shown in Fig. 4.3. A cooperativity parameter of $C = 2.5 \pm 0.5$, dephasing rate of $\gamma_\perp = 2 \pm 0.5$ ns^{-1}, loss rate of $\kappa = 77 \pm 5$ ns^{-1}, coupling rate of $g = 19.0 \pm 0.5$ ns^{-1} and

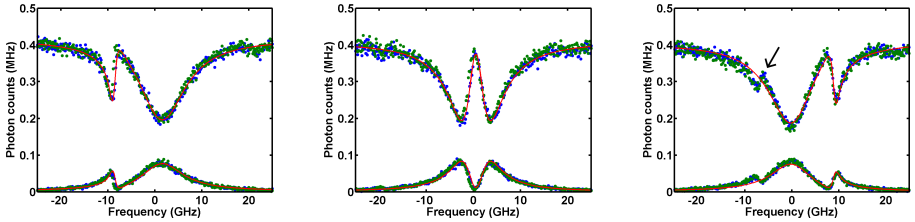

(a) Red detuned (712 mV) (b) In resonance (727 mV) (c) Blue detuned (741 mV)

Figure 4.2: *Resonant spectroscopy scans of an exciton in a cavity at 1 pW power with H polarized light. Upper (lower) curves show reflection $R(\nu)$ (transmission $T(\nu)$). Experimental data is shown in blue (green) for an upward (downward) frequency scan. In red, fits of the blue data with Eq. 2.5 and Eq. 2.6 are shown. Between brackets the bias voltage over the P-I-N junction is given. In Fig. (c) a second quantum dot on the red side of the cavity is visible (see marker).*

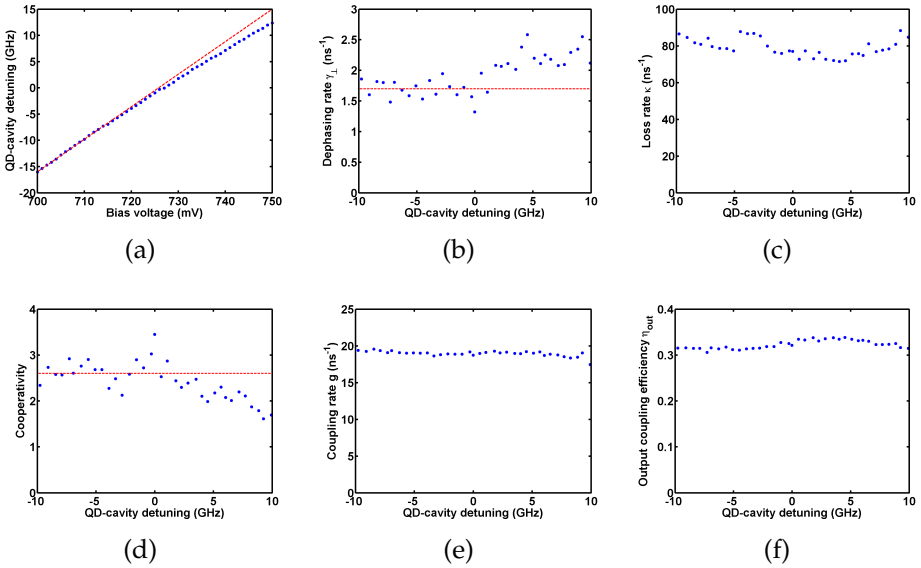

(a) (b) (c)

(d) (e) (f)

Figure 4.3: *Fitting parameters for the data set which is partially shown in Fig. 4.2 and fully shown in Fig. 4.4(b). Red dotted lines are guides to the eyes. In (a) the not fully linear Stark shift is shown. The guide to the eyes has a slope of 0.6 GHz/mV. (b) shows the dephasing rate. An upward trend is seen on the blue side of the cavity. This is accompanied by a downward trend for the cooperativity parameter shown in (d).*

output coupling efficiency $\eta_{out} = 0.32 \pm 0.02$ are found for this particular quantum dot. This places the system neither in the weak nor in the strong cavity-QD coupling regime, but in the intermediate coupling regime where $\kappa > 2g > \gamma_{\perp}$.

Figure 4.3(a) shows the Stark shift of the quantum dot, which is not fully linear, as the linear guide to the eyes indicates. In Fig. 4.3(b), the dephasing rate shows a minor upward trend on the blue side of the cavity resonance. This is accompanied by a minor downward trend on the blue side for the cooperativity parameter, since these two quantities are coupled. Blue side/red side asymmetry might indicate phonon related physics [16]. In this case the fact that another quantum dot tunes into the cavity when the main quantum dot becomes blue detuned (see Fig. 4.2(c)) might also partly explain the asymmetry.

In Fig. 4.4 colormaps of the reflectivities $R(\nu, V)$ are presented, where ν is the frequency detuning with respect to the cavity. The figure gives an overview of quantum dots that can be tuned in resonance with the cavity. In Fig. 4.4(b) the quantum dot indicated as QD1 is further investigated in this thesis. This is an exciton transition, as demonstrated with the observed finesplitting in Fig. 4.4(c). Figure 4.4(d) shows $R(\nu, V)$ for two trion transitions. These figures allow for extracting the Stark shift $d\nu/dV$. For QD1 we find $d\nu/dV \approx 0.6$ GHz/mV, for QD2 $d\nu/dV \approx 0.7$ GHz/mV and for QD3 and QD4 $d\nu/dV \approx 0.5$ GHz/mV.

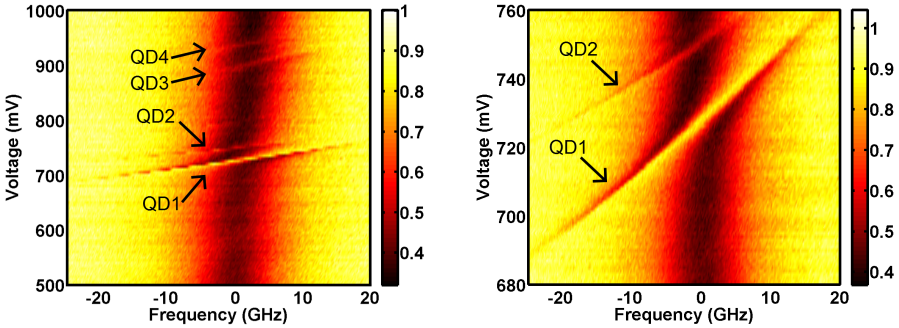

(a) Overview of quantum dots in the cavity under H polarization

(b) Two exciton transitions using H polarization, QD1 is further investigated in this thesis.

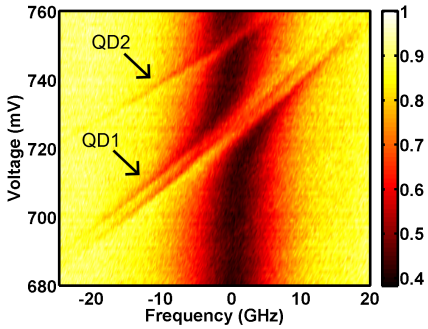

(c) Two exciton transitions using H + V polarization. For QD1, a fine-splitting of 2.5 ± 0.5 GHz is observed.

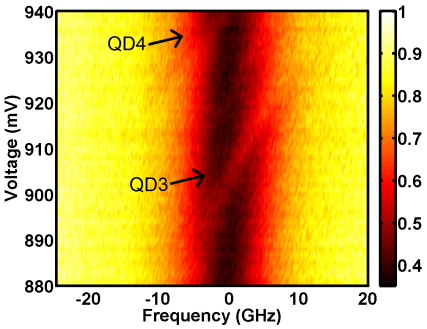

(d) Two trion transitions using H polarized light.

Figure 4.4: *Overview of reflectivities $R(\nu, V)$ of quantum dots at 1 pW, resonant with the cavity in different voltage regions and using different incoming polarizations.*

4.2 Hysteresis

Figure 4.2 showed reflection and transmission spectra at 1 pW power. When going to higher powers though, distorted line shapes appear and hysteresis is observed between an upward versus a downward frequency scan. When scanning the laser, the laser seems to be able to drag the quantum dot along in the direction of the laser scan. Scans taken with 1 nW probe laser power, showing hysteresis and line shape modification, are presented in Fig. 4.5.

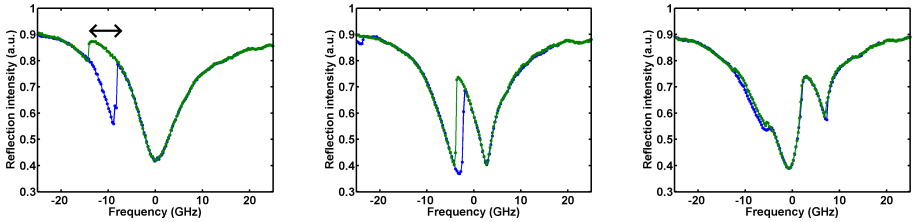

(a) Red detuned (690 mV) (b) In resonance (705 mV) (c) Blue detuned (720 mV)

Figure 4.5: *Resonant spectroscopy scans of a quantum dot in a cavity at 1 nW power in reflection $R(\nu)$. In blue (green) experimental data for an upward (downward) frequency scan is shown. Hysteresis is visible only on the red side of the cavity resonance. The width of this hysteresis, as indicated by the black arrow, will be defined as the locking range. On the blue side, where almost no hysteresis is visible, line shapes still look distorted. A scan speed of ∼30 GHz/s was used.*

A locking range can be defined by the width of the hysteresis loop when the quantum dot transition is on the red side of the cavity resonance. This locking range is indicated by the black arrow in Fig. 4.5(a). A power dependency of the locking range is shown in Fig. 4.6(a). This dependency shows linear behavior on a semi-log plot. Therefore the dependency $\Delta\nu = \Delta\nu_0 ln(1 + P/P_0)$ had been drawn as a guide to the eyes with $\Delta\nu_0 = 0.65\,\text{GHz}$ and $P_0 = 2\,\text{pW}$.

When adjusting the power, one of the experimental observations in these samples is that the quantum dots shift in frequency. A higher optical power results in a blue-shift of the quantum dots. Since the hysteresis is dependent on the cavity-quantum dot detuning, the bias voltage is adjusted to keep the cavity-quantum dot detuning constant. Figure 4.6(b) shows the applied bias voltage in order to keep the quantum dot frequency constant when varying power.

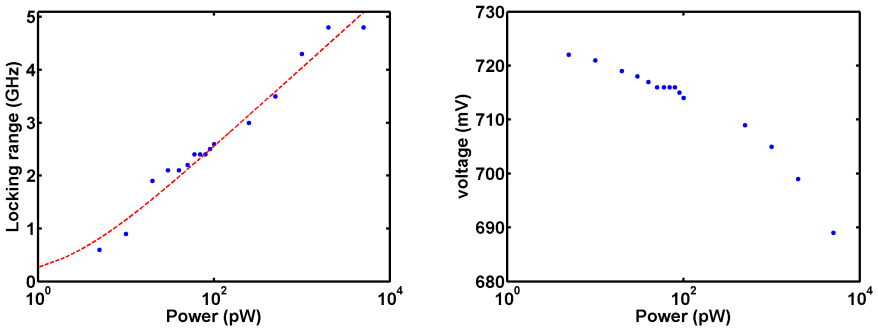

(a) Hysteresis increases non-linear with power.

(b) Applied bias voltage for a constant cavity-quantum dot detuning.

Figure 4.6: *Power dependency measurements on the hysteresis. (a) shows a red guide to the eyes with dependency* $\Delta\nu = \Delta\nu_0 ln(1 + P/P_0)$ *with* $\Delta\nu_0 = 0.65\,GHz$ *and* $P_0 = 2\,pW$.

4.3 Two-laser experiment

The power dependency measurements of the hysteresis show a clear relation between power and the amount of hysteresis. Also a blue-shift of the the quantum dot frequency was observed when higher powers are used. Unclear is yet if these two effects are related and what the physical mechanism behind the blue-shift is.

One step towards finding the physical mechanism is to see whether the quantum dot needs to be resonantly excited to be blue-shifted. In order to find out whether this is the case, a two-laser experiment was set up.

In this two-laser experiment, a 1 pW probe laser is used for low power scans. A second 1 nW pump laser is scanned step-wise over the cavity resonance and for every step a scan with the probe laser is done. The pump laser polarization is set orthogonal to the probe laser, therefore it can be filtered out before coupling into the transmission or reflection channel. In order to find the frequency of the pump laser relative to the scanning probe laser, the fast photodiode ($\nu_{response} = 150$ MHz) indicated as 'Beat' in Fig. 3.1 is used. On this detector, the pump and probe laser are interfered, creating the difference frequency. Only when the pump and probe laser have the same frequency within the frequency response of the detector, this difference frequency is small enough to be observed. Using this method, the results in Fig. 4.7 are obtained.

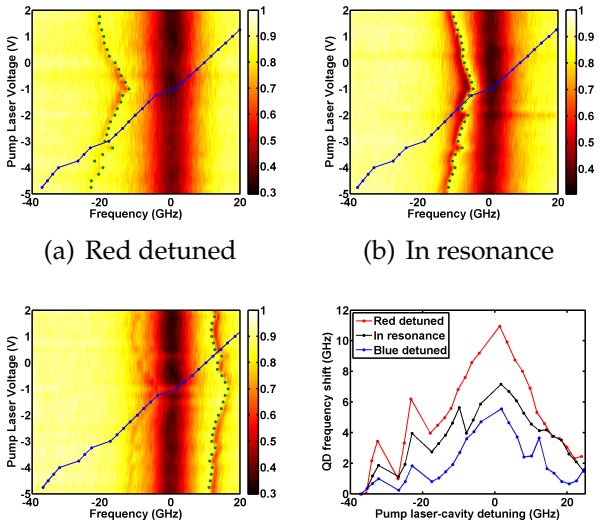

(a) Red detuned (b) In resonance

(c) Blue detuned (d) QD frequency shift

Figure 4.7: *Two-laser experiment with a pump laser (1 nW), scanned step-wise and a scanning probe laser (1 pW). (a), (b) and (c) show reflection intensity for three different QD-cavity detunings. Blue and green respectively depict the pump laser frequency and the fitted quantum dot frequency. (d) shows the quantum dot frequency shift extracted from (a) in red, (b) in black and (c) in blue.*

In Fig. 4.7, for three QD-cavity detunings, reflection intensities are presented as a function of frequency and pump laser detuning. In blue the position of the pump laser is depicted. The green dots show the fitted quantum dot frequencies for every scan with the probe laser.

A clear blue-shift of the quantum dot is observed when the pump laser becomes resonant with the cavity. This blue-shift seems to be independent of the quantum dot detuning with respect to the cavity. From these measurements we conclude that the quantum dot does not have to be excited for the blue-shift to occur.

We also note that the amount of observed blue-shift is in the same order of magnitude as the locking range observed in Fig. 4.5(a). For this scan on the red side of the cavity a locking range of $\sim$5 Ghz was observed, at a probe laser intensity of 1 nW. This gives a strong indication that the observed quantum dot blue-shift is causing the hysteresis and that during a scan, the quantum dot blue-shifts dynamically which is converted into hysteresis.

4.4 Hysteresis model

In the two-laser experiment it was observed that the quantum dot blue-shifts when a powerful pump laser becomes resonant with the cavity, and that the QD-cavity detuning does not seem to be an important factor. From this observation we hypothesize the following physical mechanism behind the blue-shift.

Due to absorption of light in the cavity, electron-hole pairs are created, which screen the applied electric field. Thereby the effective electric field is lowered, which leads to blue-shifting of the quantum dots. The simplest way to model this, is to model a frequency shift proportional with a charge build-up Q. This charge build-up is proportional with the intracavity intensity, which itself is proportional with the transmission intensity.

$$t = t(f_{laser}, f_{QD}) \tag{4.1}$$
$$Q = \beta |t|^2 \tag{4.2}$$
$$f_{QD} = f_{QD0} + \alpha Q \tag{4.3}$$

where α is a Stark shift parameter with units GHz/C, and β is a parameter stating the amount of optical power converted into charge with units C/nW. Note that this is the amount charge per transmitted nW, and not the power in front of the objective which is used extensively in this thesis. These equations are coupled and in order to simulate the hysteresis, for every step with the scanning laser, Q is calculated by iterating through the equations a set amount of times.

Figure 4.8 shows the experimental observations on hysteresis in comparison with obtained simulations. These simulations show that an intracavity intensity dependent blue-shift, will indeed result in hysteresis. This hysteresis is only present on the red side of the cavity. On the blue side of the cavity, the line shapes are still modified but no hysteresis is visible. Although no hysteresis is present in the simulation on this side of the cavity, the line shape in Fig. 4.8(f) does not exactly resemble the experimentally obtained line shape shown in Fig. 4.8(c). Manually modifying the fit parameters has not resulted in a better resemblance between experiment and simulation.

It should be noted that for every simulation in Fig. 4.8 other fit parameters were used. These parameters have been chosen for best resemblance with

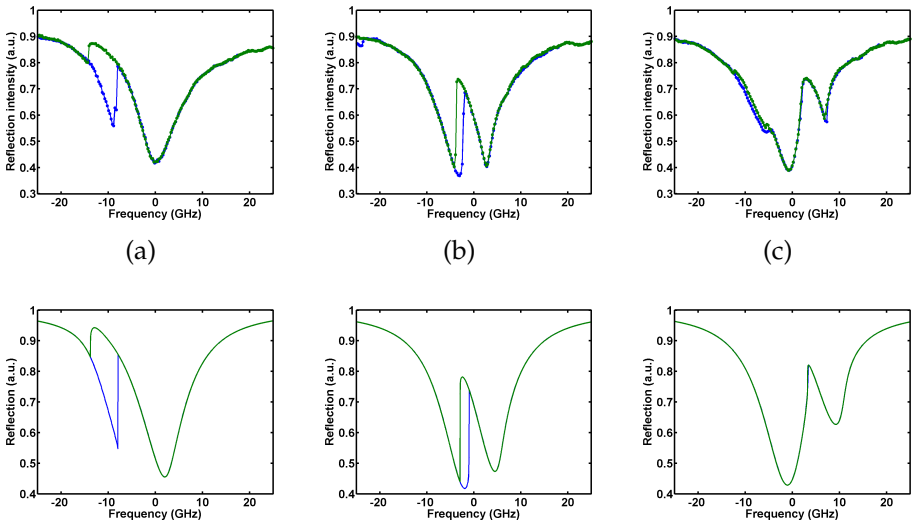

(a) (b) (c)

(d) f_{QD0} = -14.0 GHz, $\alpha\beta$ = 102 GHz/nW, C = 2.7, $\gamma_\perp$ = 1.7 ns^{-1}, η_{out} = 0.33, κ = 80 ns^{-1}

(e) f_{QD0} = -3.6 GHz, $\alpha\beta$ = 56 GHz/nW, C = 1.0, $\gamma_\perp$ = 5.0 ns^{-1}, η_{out} = 0.37, κ = 80 ns^{-1}

(f) f_{QD0} = 3.0 GHz, $\alpha\beta$ = 89 GHz/nW, C = 1.2, $\gamma_\perp$ = 7.0 ns^{-1}, η_{out} = 0.35, κ = 80 ns^{-1}

Figure 4.8: *(a), (b) and (c) show the experimental data of Fig. 4.5 for easy comparison to the simulations in (d), (e) and (f).*

the experiments. A possible explanation for the differing fit parameters between the figures could be that the relation between Q and $|t|^2$ is not linear. An argument for that being the case is the observed non-linearity between the power and locking range in Fig. 4.6(a).

4.5 Time dynamics

In the previous section it was shown that the observed blue-shift, which increases with intracavity power, explains the observed hysteresis. This blue-shift was attributed to a charge build-up in the micropillar structure. In this section, time resolved measurements on the blue-shift are performed in order investigate the timescale of the charge build-up.

For these time resolved measurements, the probe laser (1 nW) was set stationary on the red or blue side of the cavity. For different QD-laser detunings, the laser was turned off and on. When the laser is turned on, the quantum dot starts blue-shifting, causing a change in the reflection signal.

For three different QD-laser detunings the results of these measurements are shown in Figs. 4.9(c) and 4.9(d). The three curves correspond to the cases drawn in the accompanying sketches in Figs. 4.9(a) and 4.9(b). Note that for clarity, in the sketches the laser has been detuned instead of the quantum dot. However, these sketches still correctly show the different QD-laser detuning cases.

For the sketches in Figs. 4.9(a) and 4.9(b), in red the quantum dot reflection spectrum has been drawn when the laser is off. When the laser is turned on, the quantum dot starts blue-shifting and the maximally blue-shifted curve has been drawn in blue. The black dotted lines show the laser position, indicating the QD-cavity detuning for the three different cases. The shapes of the three experimentally measured curves can be explained by looking at the sketch, and at one of the laser frequencies while shifting the quantum dot from the red curve to the blue curve. From this experiment we extract a typical timescale of the blue-shifting, and therefore of the charging, of $\sim$1 ms.

With the charging model described by Eqs. 4.1, 4.2 and 4.3, the time resolved measurments have been simulated in Figs. 4.9(e) and 4.9(f). For simulation of these time resolved curves, parameters similar to the ones measured during the 1 pW scans in Fig. 4.3 have been used: $C = 2.5, \gamma_\perp = 1.7\ \mathrm{ns}^{-1}, \kappa = 77\ \mathrm{ns}^{-1}, \eta_{out} = 0.31, \alpha\beta = 78\ \mathrm{GHz/nW}$. Between the curves, only the quantum dot frequency was varied. Some key features of the measured curved could be reproduced, but not all. The issue of the linear relation between Q and $|t|^2$ that possibly applied to the hysteresis simulations, will also apply here which might explain discrepancies between measurements and simulations.

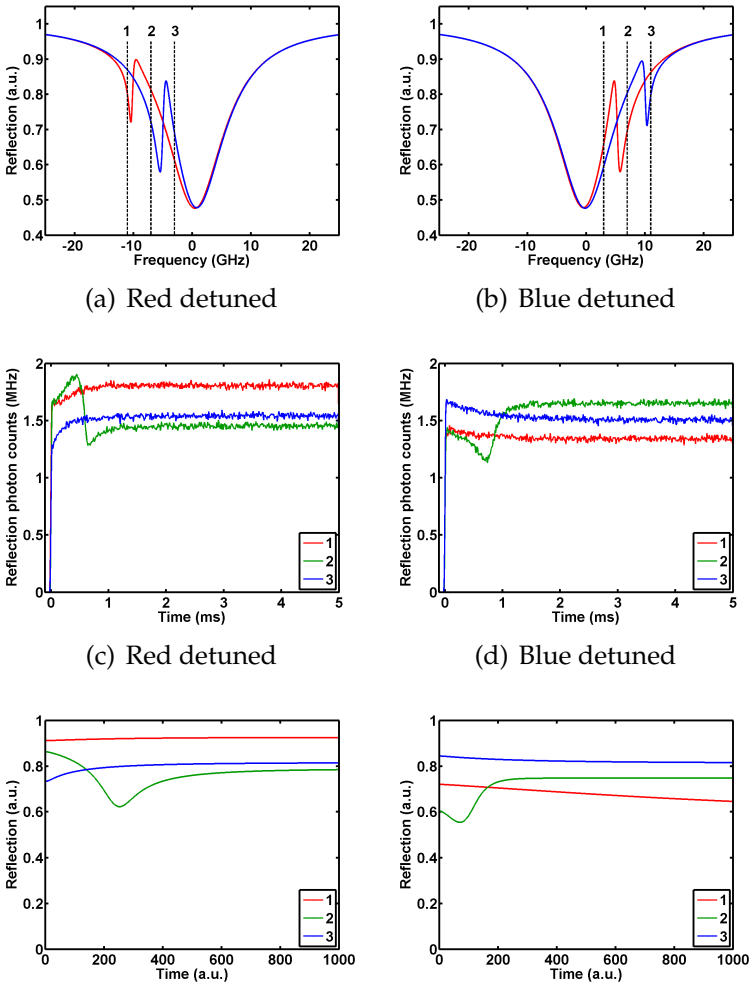

(a) Red detuned (b) Blue detuned

(c) Red detuned (d) Blue detuned

(e) Red detuned (f) Blue detuned

Figure 4.9: *Time resolved dynamics of the blue-shift. (a) and (b) show a sketch of the situation. The red curves are reflection spectra in absence of the laser. The blue curve shows the steady-state situation when the laser is on. In black the different spectral positions of the laser are shown with respect to the quantum dot. Note that during the experiment the quantum dot was detuned instead of the laser. (c) and (d) show measured time resolved reflection curves. (e) and (f) present simulated reflection curves using the model described in section 4.4.*

4.6 Discussion

In this section some of the results will be discussed in more detail.

In section 4.4 it was proposed that a charging model could explain the observed blue-shift of which we concluded that it explains the blue-shift. Some questions have remain unanswered until now. It is still unclear where exactly the light is being absorbed and where the free charges are created. The photons do not have enough energy to excite electrons over the GaAs bandgap, but they might be exciting electrons in the doped layers.

The observed millisecond timescale is rather slow for carrier dynamics in semiconductors which is typically on the picosecond scale. However, if charge traps are present, this timescale could possible be lengthened to milliseconds. Charge traps in the vicinity of quantum dots have previously been studied [17]. In this reference, up to four charge traps within 50 nm were observed. These charge traps caused discrete frequency shift steps of up to 3 GHz per filled charge trap. In our sample we see a very continuous shift of maximally a cavity width with resonant excitation. This indicates that there are many charges involved which are trapped quite far away from the quantum dots.

In the micropillar samples the oxide aperture is not conductive and this might lead to a charge build-up around the aperture layer. In order to test this hypothesis, the presence of blue-shift outside the cavity region where no oxide aperture is present was tested. This cannot be done resonantly, but photoluminescence has to be used. With a spectrometer the quantum dot frequency could be determined. Doing photoluminescence measurements on quantum dots in the cavity region still showed blue-shift with power. However, outside the cavity region where no oxide aperture is present, this blue-shift was not observed. This proves that indeed the oxide aperture plays a role in the charge build-up.

Another physical mechanism that has been considered is dynamic nuclear polarization (DNP). This DNP model imposes that if a quantum dot is optically excited, the electron spin from the created exciton or trion can be transferred by a flip-flop process to an atom in the quantum dot. This way nuclear spin can be built up in the quantum dot, creating a nuclear magnetic field, thereby Zeeman shifting the electronic transitions of the quantum dot [18]. More intracavity optical field results in a higher nuclear polarization, which results in a higher Zeeman shift. Scanning hysteresis

has been observed and attributed to DNP in literature before [19].

DNP is considered an unlikely candidate for our observed blue-shift. There are some simple arguments that can rule out DNP with high certainty. A first argument is that applying a magnetic field in the Voigt configuration up to 1 T does not give different results for the observed hysteresis. Another argument is that we only observe a blue-shift, while a nuclear polarization can be build up in both directions. Therefore we should also be able to observe a red-shift, which is not the case. The final and most important argument against DNP is the fact that the observed blue-shift increases when a non-resonant laser is added, which is not exciting the quantum dot.

The hysteresis simulations show some minor discrepancies with respect to the experimental results. The modified lineshapes on the blue side of the cavity resonance could not be fully replicated. Also with the time resolved measurements some differences between the experimental results and the simulations are seen. A couple of improvements to the model can be made, which might possibly correct these discrepancies. First a non-linear relation between Q and $|t|^2$ could be used. This is follows from the non-linear relation between intensity and amount of hysteresis shown in Fig. 4.6(a). In Fig. 4.3 it was shown that some fitting parameters show a detuning dependency, possibly related to phonon physics. Therefore a second improvement that can be done is incorporating detuning dependent parameters. A third and last improvement is adding a saturation coefficient. This saturation coefficient might be necessary due to the fact that the one photon per quantum dot lifetime intensity is $\sim$1 nW. Therefore some photons cannot interact with the quantum dot since it might already be excited, resulting in a lower cooperativity parameter.

The charging model seems valid, though a key experiment to really prove the hysteresis effect is caused by charge build-up is difficult. Trying to measure quantum dot related currents through the sample have been unsuccessful so far. Another approach would be to use a set of samples with oxide apertures in different sizes and dimensions. However, we do not posses such a set and the sample growing process will likely be a lengthy process.

Chapter 5

Future outlook

In this chapter two experiments will be described, for which first steps have been taken and first measurements are done. Both experiments show interesting and promising results, but further work is needed.

5.1 Photon correlations

Going to the single photon level is essential for quantum experiments. In this experiment, photon correlation measurements on a quantum dot inside a micropillar cavity have been performed.

5.1.1 Setup

For these correlation measurements, using a PID loop on a transmission fringe of the 250 MHz Fabry-Perot cavity, the probe laser was set stationary on the cavity resonance ($f_{laser} = f_{cavity}$). Next, the quantum dot was tuned in resonance with the laser by voltage tuning, resulting in $f_{laser} = f_{cavity} = f_{QD}$. Correlations in a single channel were measured using a Hanbury-Brown-Twiss (HBT) experiment. The channel is split using a 50:50 beam splitter and fed into two single-photon counting modules (SPCM). Both SPCMs are connected to a Becker & Hickl SPC330 time-correlated single photon counter (TCSPC) card. One of the SPCMs is connected to a start input, starting the counter, while the other is connected to the stop input, stopping the counter. This results in an autocorrelation of the photon

channel. Two different SPCMs were used in these experiments, Perkin Elmer SPCM-AQR-14-FC SPCMs with a timing jitter of ∼2 ns and a quantum efficiency of ∼25% at 940 nm. The other SPCMs are ID Quantique ID100-MM50 SPCMs with a lower timing jitter of ∼100 ps, but also a lower quantum efficiency of ∼3% at 940 nm.

5.1.2 Results

Results for this experiment in transmission are shown in Fig. 5.1. In the transmission channel photon bunching is observed. As a reference, if the quantum dot is tuned out of the laser resonance, neither bunching nor anti-bunching is observed.

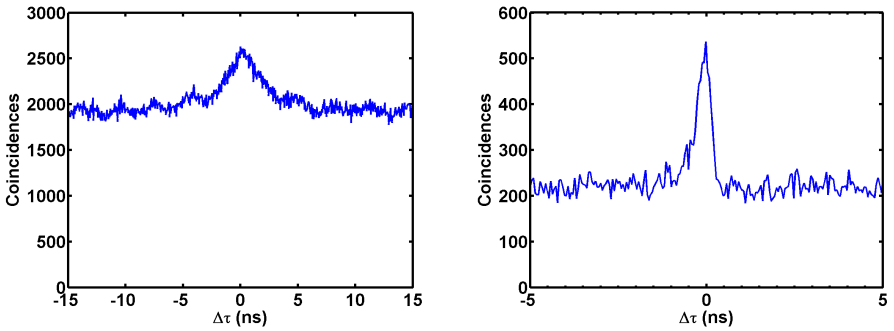

(a) High jitter detector (∼3 ns), 150 s integration time

(b) Low jitter detector (∼100 ps), 18 minutes integration time.

Figure 5.1: *Transmission autocorrelation at 1 nW power, bunching is observed. The ∼3 ns oscillations in the autocorrelation are measurement artifacts, originating from the TCSPC card.*

Next, we take a look at the reflection channel. However, doing the same experiment in reflection is somewhat more difficult, due to the reflection background of ∼40% of the incoming light on the sample (see for example Fig. 4.2 where the minimum reflection is actually ∼50%). This is light that is reflected on the air-DBR interface whereby polarization is maintained. Trying to measure correlations in the reflection channel, despite this reflection background, has not resulted in a visible bunching or anti-bunching. However, the reflection correlation can be measured using a cross-polarization technique. This technique allows for collection of photons in a channel that have all had an interaction with the quantum

dot, thereby blocking the reflection background. The cross-polarization technique is described in Appendix A. The autocorrelation of the cross-polarized reflection signal is shown in Fig. 5.2.

Lastly we take a look at the correlation between the reflection and transmission channel. Both channels are cross-polarized and each directly fed into an SPCM, which is then connected to the TCSPC card. The results of this measurement are presented in Fig. 5.3.

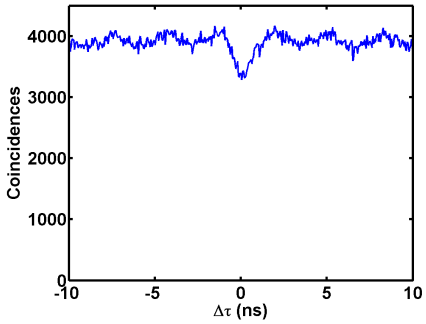

Figure 5.2: *Autocorrelation of the cross-polarized reflection channel at 1 nW power with the Perkin-Elmer detectors. Anti-bunching is observed.*

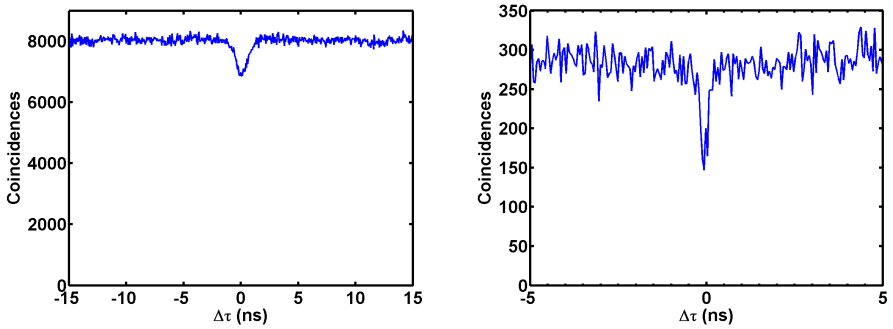

(a) High jitter detector (∼3 ns), 60 s integration time

(b) Low jitter detector (∼100 ps), 2 hours integration time.

Figure 5.3: *Correlation between the cross-polarized reflection and cross-polarized transmission channel at 600 pW. Anti-bunching is observed.*

5.1.3 Intuitive picture

The results can be qualitatively explained by a simple model depicted in Fig. 5.4. In a single quantum dot lifetime, the quantum dot can only interact with a single photon. If a Fock state of n photons is injected in the cavity QED system, only the first photon can interact with the quantum dot, which is then reflected. The other photons cannot interact with the quantum dot anymore and only 'see' an empty cavity and will therefore be transmitted. If a Poissonian distribution with mean photon number N and therefore standard deviation $\Delta N = \sqrt{N}$ is input in the system. The transmitted distribution is shifted to a mean photon number of N-1, but still has a standard deviation of $\Delta N = \sqrt{N}$. This transmitted distribution is therefore super-Poissonian and therefore bunched, giving a qualitative explanation for the observed bunching in transmission.

The observed anti-bunching in the cross-polarized measurements can also be explained by the fact that the quantum dot can only interact with a single photon at a time. Because we are only looking at photons which have interacted with the quantum dot using the cross-polarizers, two photons can never be detected at the same time.

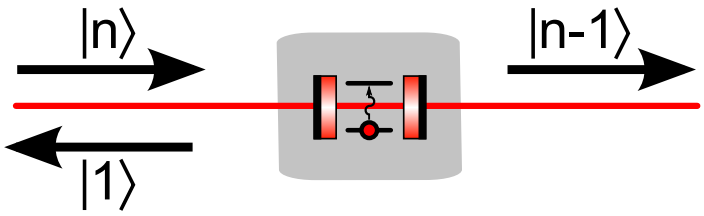

Figure 5.4: *For an incoming n photon state, the first photon is reflected by the quantum dot and a n-1 state is transmitted, resulting in a bunched photon distribution in transmission.*

5.1.4 Outlook

As a first approximation, the described model looks reasonable. It explains bunching in transmission and anti-bunching in reflection which we observe during measurements. On the other hand this is a model that neglects a lot of the cavity QED physics and is therefore probably too simple. If the cavity QED system is described by the Jaynes-Cummings model,

the laser-cavity-quantum dot detunings become much more important as a way to climb the Jaynes-Cummings energy ladder [8, 9]. This model predicts that it should be possible to create an emitter of n-photon states using a cavity QED system in the strong coupling regime.

The next step that could be taken with the correlation measurements is scaling up to four SPCMs. This way the third and fourth order correlation function can be calculated and with these higher order correlation functions, the presence of a particular Fock state can be resolved.

5.2 Quantum dot coherence measurements

Another experiment we performed is an interference experiment. Using this experiment, the coherent fraction of light that has interacted with a quantum dot can be measured.

5.2.1 Setup

For this experiment the setup in Fig. 5.5 has been used. Using the scanning probe laser, a usual resonant spectroscopy scan is done. The transmitted signal is interfered with the original probe laser by means of a bypass. Due to the fact that the laser is scanning with a speed of $\sim$30 GHz/s, while the optical path length difference between the transmission path through the sample and the bypass is in the order of $\sim$10 m, this results in a constant frequency beat on the order of 100 Hz. However, this will only be the case if the in the transmission path is still coherent with the bypass. Otherwise, if the quantum dot interaction is incoherent, the loss of coherency will cause the two channels to add up incoherently and no beat will be visible.

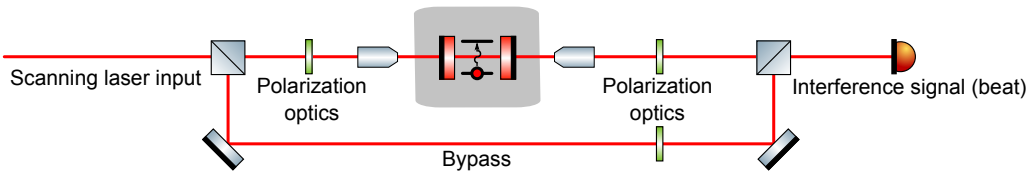

Figure 5.5: *Interference setup for coherence measurements on quantum dot transitions.*

5.2.2 Results

This experiment has been performed for both the exciton and the trion transition in Fig. 5.6, for both a normal scan and a cross-polarized scan.

For the normal scans in Figs. 5.6(a) and 5.6(b), we see that light that has not interacted with the quantum dot, but is transmitted through the cavity produces a beating signal. The presence of a beating signal shows that the light is still coherent with the bypass channel. For light that has interacted with the quantum dot, we use the cross-polarization technique shown in Appendix A. For these scans in Figs. 5.6(c) and 5.6(d), we only observe a beating signal for the exciton transition. For the trion transition, no beating is observed, showing that the light has interacted incoherently with the quantum dot.

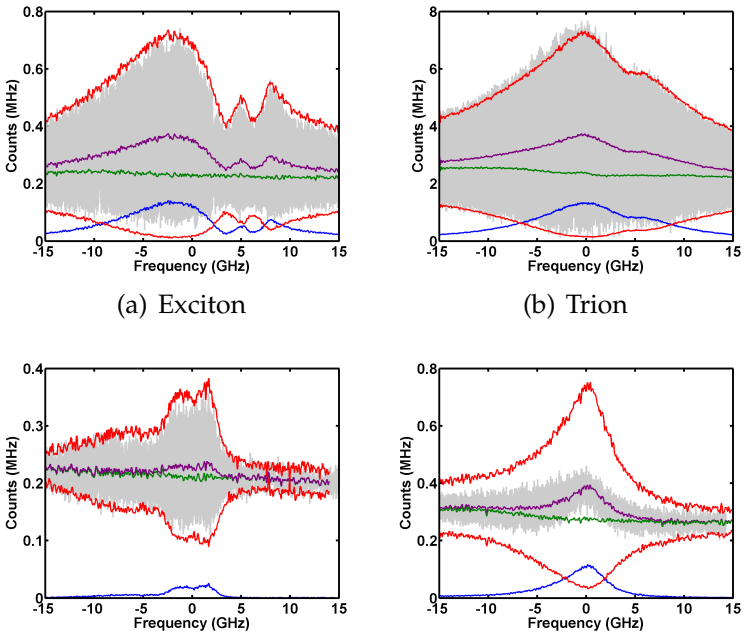

(a) Exciton (b) Trion

(c) Exciton cross-polarized (d) Trion cross-polarized

Figure 5.6: *Interference measurement between the transmission signal and the original probe laser. In green the probe laser intensity is shown and blue shows the transmission channel intensity. Purple represents the incoherent sum of those two and red shows the envelope of the coherent sum. Gray shows the actual data of the interfered transmission signal and probe laser.*

5.2.3 Outlook

With the beating signal we seem to be able to precisely determine the fraction of coherent interaction between light and a quantum dot. This allows for a detailed study of decoherence processes in quantum dots. For improvement of the SNR, some minor experimental improvements have to be done to reduce phase and frequency jitter due to vibrating fibers.

Chapter 6

Conclusion

The key result presented in chapter 4 is the resolved origin of scanning hysteresis with quantum dots in micropillar cavities. This scanning hysteresis has been observed for resonant spectroscopy scans and is only visible on the red side of the cavity resonance. The hysteresis exhibits a strong power dependence, where a higher power results in more hysteresis. By performing two experiments, the origin of the hysteresis has been found. The first experiment involved a two-laser experiment with a high power pump laser and an orthogonally polarized low power probe laser. The experiment showed a blue-shift of the quantum dot transition, proportional with the intracavity optical power. This blue-shift was independent of the cavity-quantum dot detuning. The second experiment involved time resolved measurements on this blue-shift. This experiment showed quantum dots shifting in frequency on a millisecond timescale. These observations have led to a simple mathematical model which is able to fully reproduce the hysteresis and a part of the time resolved traces. To turn the mathematical model into a physical model, charging is proposed to be origin of the blue-shifting by means of the quantum confined Stark effect. In chapter 5 a future outlook is given which shows first results on photon correlation and interference measurements. Both experiments in this chapter show interesting and promising results for future research.

Appendix A

Polarization degenerate solid-state cavity QED

In this appendix, a study on quantum dots in a polarization degenerate cavity has been included. In this study, cross-polarization techniques have been used extensively. Also in Ch. 5 of this thesis the cross-polarization technique was used. Detecting photons in a cross-polarized channel, requires excitation of both orthogonal, fine-split exciton transitions. This is shown as the 45° case in Fig. 2(d) of this appendix.

Polarization degenerate solid-state cavity QED

Morten P. Bakker,[1] Ajit V. Barve,[2] Thomas Ruytenberg,[1] Wolfgang Löffler,[1] Larry A. Coldren,[2] Dirk Bouwmeester,[1,2] and Martin P. van Exter[1]

[1] *Huygens-Kamerlingh Onnes Laboratory, Leiden University, P.O. Box 9504, 2300 RA Leiden, The Netherlands*

[2] *University of California Santa Barbara, Santa Barbara, California 93106, USA*

(Dated: October 17, 2014)

Cavity quantum electrodynamics experiments are presented with charge-controlled quantum dots (QDs) coupled to a polarization degenerate microcavity and investigated through resonant reflection and transmission spectroscopy. This enables control of the full polarization degrees of freedom, which we demonstrate by measuring interference of the two fine-structure split transitions of a neutral QD that are found to evolve fully coherently, in agreement with theory. We also study a negatively charged QD where the ability to use arbitrary polarizations enables identification of the more complex dynamics and decoherence processes.

Quantum dots (QDs) embedded inside microcavities are of interest for single-photon switches [1–4] and hybrid optical-solid-state quantum information schemes [5, 6]. Micropillars are an excellent candidate as they combine mode-matching to external fields, access to the Purcell and strong-coupling regimes, QD charge and Stark shift tuning, and polarization control of the cavity modes [3, 7–12].

In this letter we report on charge controlled quantum dots coupled to a polarization degenerate microcavity; a system that enables full utilization of the polarization degrees of freedom as required in quantum information applications. The microcavity (polarization splitting <3 GHz) consist of two distributed Bragg reflectors, an aperture region for transverse mode confinement, and a λ thick cavity layer, containing InAs self-assembled QDs embedded inside a PIN-diode structure [13–15]. Further details on the sample structure and characterization can be found in the Supplemental Material section I. The setup, an optical, and an electron microscope image of the sample are shown in Fig. 1.

Through resonant spectroscopy using arbitrary polarizations in the excitation and detection paths, we investigate the coherence properties of neutral and singly charged QD transitions. First we study the coherent interaction of charge-neutral quantum dot transitions with resonant laser light and give a theoretical description. Then we investigate a singly charged QD and study its more complex dynamics.

The lowest energy levels of a neutral QD are depicted in Fig. 2 (e). Due to asymmetry in the shape of the QD, the electron-hole exchange interaction leads to a fine-structure splitting of the excited states ($\sim$ 3 GHz for the QD under study), and a neutral ground state is coupled to two excited states by two linear orthogonally polarized transitions. We tune the QD transition through the cavity resonance by the quantum confined Stark effect, induced by the applied bias voltage across the active region [16, 17]. In the resonant reflection measurements in Fig. 2 (a), the QD – cavity anti-crossing as a hallmark of strong QD – cavity coupling is clearly visible. Low laser power (P_{laser} = 1 pW) is used in order to avoid saturation of the QD transition, charging and dynamical nuclear spin polarization effects. Fig. 2 (b, c) show reflection and transmission spectra for a voltage V=0.725 V, where QD1 is tuned into resonance with the cavity. The spectra are recorded for three linear polarizations that couple with the low frequency QD transition ($\theta_{in} = 0°$), the high frequency QD transition ($\theta_{in} = 90°$), or both QD transitions ($\theta_{in} = 45°$). Additionally we show spectra when a crossed polarizer is used in the transmission path in Fig. 2 (d).

For 0° and 90° polarization we observe that the quantum dot is able to restore high cavity reflectivity with near-unity fidelity, but this effect appears to be reduced

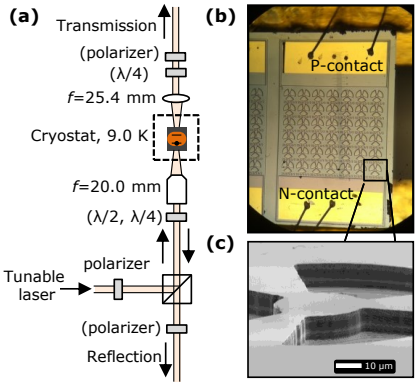

FIG. 1. (a) Schematic of the setup. Light is coupled into a microcavity mode and the reflection and transmission spectra are recorded using single-photon avalanche photodiodes. The elements with names between brackets can be introduced for polarization analysis with either linear or circularly polarized light. $\lambda/2$ ($\lambda/4$): half- (quarter-) waveplate. (b) Optical microscope image of a sample and (c) Electron micrograph of the cavity region.

for 45°. In the cross-polarized transmission spectra in Fig. 2(d), we see that for 0° and 90° the light matches the natural polarization axes of the QD and it is maintained, resulting in a very low signal. For 45° incoming polarization the transmission is significant however. In the following, we develop a theoretical model to gain insight into the dynamics.

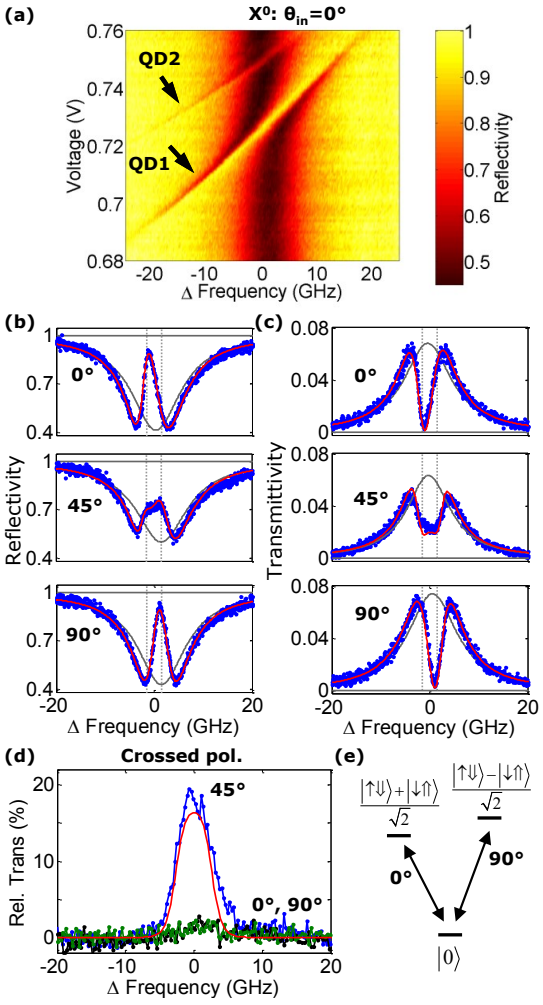

FIG. 2. (a) Reflectivity measurement of two neutral QDs as function of the scanning laser frequency and applied voltage. The incoming polarization $\theta_{in} = 0°$, $P_{laser} = 1$ pW and $\lambda \approx 940$ nm. Panel (b, c) show reflectivity and transmittivity spectra of QD1 recorded at $V = 0.725$ V for various incoming linear polarizations. Blue points: experimental data. Red line: fitted curve using Eqs. 1 and 2. Grey curve: empty cavity. Vertical dashed lines: frequencies corresponding to the two fine-split transitions. (d) Transmittivity spectra when a crossed polarizer is used with respect to the incoming polarization. The red line is calculated using Eqs. 1 and 2 and the parameters obtained from the fits in (b, c). (e) Energy level diagram of the ground-state and lowest energy excited states of a neutral QD.

The transmission amplitude through a cavity with a coupled QD is given by [3, 18, 19]:

$$t = \eta_{out} \frac{1}{1 - i\Delta + \frac{2C}{1-i\Delta'}}, \tag{1}$$

where $\Delta = 2(\omega - \omega_c)/\kappa$ is the relative detuning between the laser (ω) and cavity (ω_c) angular frequencies, $C = \frac{g^2}{\kappa\gamma_\perp}$ is the device cooperativity, $\Delta' = (\omega - \omega_{QD})/\gamma_\perp$ is the relative detuning between the laser and QD transition (ω_{QD}) and η_{out} is the output coupling efficiency. κ is the total intensity damping of the cavity, $\gamma_\perp$ is the QD dephasing rate and g is the QD-mode coupling strength. We obtain close to perfect mode-matching, and therefore the total transmittivity through the cavity is given by $T = |t|^2$, and the total reflectivity is given by $R = |1 - t|^2$. A more detailed description of Eq. 1 is provided in Supplemental Material section II.

An important figure of merit of the QD-cavity system is the cooperativity parameter C. By fitting our model to the experimental data in Fig. 2 for $\theta_{in} = 0°$ and $\theta_{in} = 90°$, we find $C = 2.5 \pm 0.5$, a value similar to previously reported [3]. We also obtain $\gamma_\perp = 2.0 \pm 0.5$ ns^{-1}, which corresponds to a total dephasing time $\tau = 500$ ps, and total cavity damping rate $\kappa = 77$ ns^{-1}, which corresponds to a quality factor of $Q \sim 2.6{*}10^4$ [15]. Since $\gamma_\perp < 2g = 39$ ns$^{-1} < \kappa$, this places the system at the onset to the strong-coupling regime.

Now we have to take account for the fine-structure splitting of the neutral QD transitions in the polarization-degenerate cavity, hence we write the transmission of the system in terms of a Jones matrix $\mathbf{t}(\omega) = \begin{pmatrix} t_x(\omega) & 0 \\ 0 & t_y(\omega) \end{pmatrix}$. The measured transmittivity therefore depends on the input and output polarization as

$$t_{\theta_{out},\theta_{in}}(\omega) = \mathbf{e}_{out}^{\dagger} \mathbf{t}(\omega) \mathbf{e}_{in}, \tag{2}$$

where $\boldsymbol{e_i} = (cos(\theta_i), sin(\theta_i))$ defines the linear input/output (i =in/out) polarization with angle θ_i. This model assumes that when the two transitions are excited simultaneously ($\theta_{in} = 45°$), coherence in the system is fully maintained leading to quantum interference between the transmission amplitudes t_x and t_y. In an incoherent system we would obtain a classical mixture of the excited states, making such interference impossible.

To further explore the validity of Eq. 2, we show in Fig. 3 (a, b) reflection and transmission spectra for $\theta_{in} = 45°$, while $\theta_{out} = \theta_{in} + 90° + \Delta\theta_{out}$ is varied. For $\Delta\theta_{out} = 0°$, the crossed polarizer condition, the transmission and reflection spectra consist of two partially overlapping Lorentzian lines split by ∼3 GHz. The phase

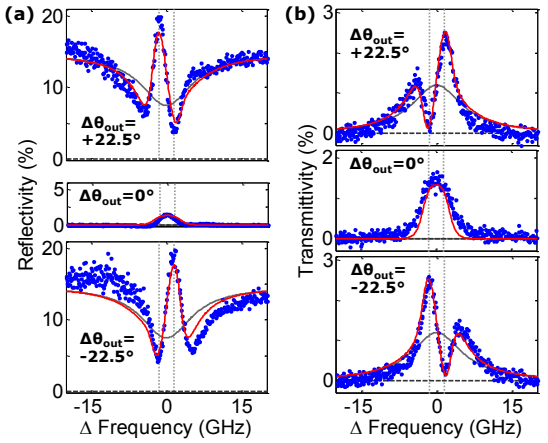

FIG. 3. Resonant (a) reflection and (b) transmission spectroscopy with a neutral QD for $\theta_{in} = 45°$ and for various $\theta_{out} = \theta_{in} + 90° + \Delta\theta_{out}$. Blue dots: experimental data. Red lines: predicted curves using Eqs. 1 and 2 and the parameters obtained from the fits in Fig. 2 (b,c). Grey lines: curves corresponding to an empty cavity. Vertical dashed lines mark the two transitions split by the fine-structure interaction.

difference between these two resonances becomes apparent for the $\Delta\theta_{out} = +22.5°$ $(-22.5°)$ spectra, which can be seen as the *coherent sum* of the $\Delta\theta_{out} = 0°$ and the $\Delta\theta_{out} = +45°$ $(-45°)$ spectra, where the latter only contains the high (low) frequency transition. All the red curves in Fig 2 and 3 are produced with the same parameters for C, κ and $\gamma_\perp$ and fit the experimental data very well. We therefore conclude that the neutral exciton forms a highly coherent three level system.

Now we turn to a different QD in the same polarization degenerate cavity, but operated in a voltage regime where it is singly negatively charged. This system is of particular importance in quantum information as the optical transitions are polarization degenerate (see Fig. 4 (a)), due to the absence of electron-hole exchange interaction, and enables coherent control of the resident electron spin if a small in-plane magnetic field is applied (Fig.4 (b)). We first focus on the data without external magnetic field shown in Fig. 4 (c, d), which shows transmission spectra when circularly (σ^+) or linearly (X) polarized light is coupled into the cavity and transmitted light of the same (i.e., parallel) polarization is recorded. We define the contrast as $(|t_c|^2 - T)/|t_c|^2$, with the measured transmittivity T and the calculated transmittivity without QD $|t_c|^2$. In contrast to the neutral QD case, we observe here a strongly reduced contrast of the QD resonance, which is $\sim 19\%$ when circularly polarized light is used and $\sim 26\%$ for linear polarization.

In addition, we show in Fig. 4 (e) the cross-polarized transmitted intensity normalized to the maximum cavity transmission: For circular (σ^+ and σ^-) polarization we observe negligible transmission, indicating that circular polarization remains unchanged. Surprisingly, for linear (X and Y) polarization, we observe that about 10% of the light is transmitted relative to $|t_c|^2$.

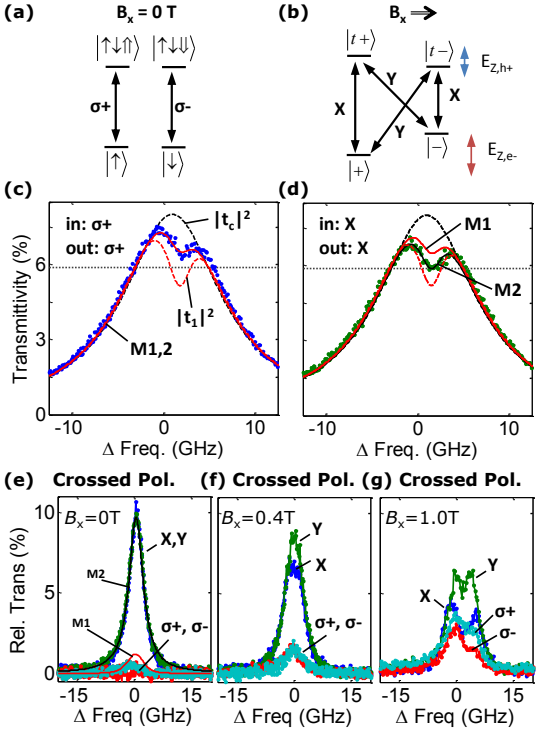

FIG. 4. (a) Energy level diagram of a singly charged QD without (a) and with (b) an external in-plane magnetic field B_x. Transmission spectra for $B_x = 0$ T and $P_{laser} = 10$ pW are shown for circular (c) and linear (d) polarization, analyzed with a parallel polarizer. The red line in (c) is a fit of Eq. 4 to the data; which is then used to predict the experimental data in (d) and (e, crossed polarizer), shown by the black line. Red through line in (d,e) is the prediction as if system were fully decoherent. Black (red) dashed curves: empty (coupled) cavity calculations. Panel (f, g) show cross-polarized transmission with an in-plane magnetic field.

We extend now our theoretical coherent model in an effort to explain these findings. The charged excitonic transitions are shown in Fig. 4 (a): The ground state consists of the two spin eigenstates, oriented in the out-of-plane direction, which couple with two corresponding trion lowest-energy excited states by degenerate circularly polarized optical transitions carrying spin $\sigma^\pm = \pm 1$. $t_1^\pm \equiv t_1$ are the corresponding transmission amplitudes of $\sigma^\pm$ polarized light, and $t_c^\pm \equiv t_c$ those for the case of an empty cavity. Since we do not control the electron spin state it can be in any random state

$|\phi_{spin}\rangle = \alpha|\uparrow\rangle + \beta|\downarrow\rangle$. With the incoming photon state $|\phi_{in}\rangle = \gamma|+\rangle + \delta|-\rangle$ we obtain for the input quantum state $|\Psi_{in}\rangle = |\phi_{in}\rangle \otimes |\phi_{spin}\rangle$. The spin-selective interaction with the cavity-QD system entangles the photon with the electron spin and we obtain

$$|\Psi_{out}\rangle = t_1\gamma\alpha|+\uparrow\rangle + t_c\gamma\beta|+\downarrow\rangle + t_c\delta\alpha|-\uparrow\rangle + t_1\delta\beta|-\downarrow\rangle. \quad (3)$$

We then project this output state onto the detected polarization $|\phi_{out}\rangle = \gamma'|+\rangle + \delta'|-\rangle$, and take the trace over the electron spin to obtain the projected transmission:

$$T = |t_1\gamma\gamma' + t_c\delta\delta'|^2|\alpha|^2 + |t_c\gamma\gamma' + t_1\delta\delta'|^2|\beta|^2. \quad (4)$$

We see that purely circular polarized light should pass the cavity unmodified, and can therefore be fully blocked by a crossed polarizer ($\gamma\gamma' = \delta\delta' = 0$), which is what we observe experimentally in Fig. 4 (e). We therefore use the data in Fig. 4 (c) to fit our model (M1), shown by the red through line, and obtain cavity-QD coupling and QD dephasing parameters. We obtain $C = 0.12$ and $\gamma_\perp = 9.5$ ns^{-1}, for the balanced case $|\alpha|^2 = |\beta|^2 = 0.5$. One explanation for this fast dephasing is an efficient cotunneling process across the 20 nm electron tunnel barrier, which is expected to be more pronounced for the flatter conduction band here compared to the neutral QD case presented before. A sample design with a thicker tunnel barrier could reduce this dephasing channel. This fast nonradiative dephasing also reduces the cooperativity, which, however, might also be reduced due to low spatial overlap between the QD and the cavity mode.

Now let us turn to the linear-polarization data shown in Fig. 4 (d, e), where the model prediction is shown by black lines. In (d) we see a significant discrepancy between the data and our model, and in (e), the cross-polarized transmission signal for X and Y is much larger than expected. This indicates additional dephasing processes take place that cause linear light to become partly circularly polarized.

We now introduce a tentative model (M2) that describes the spin-exciton system as if it were fully decoherent. Since we do not control the electron spin state, the transmission spectrum is the average of a coupled ($|t_1|^2$) cavity and an uncoupled ($|t_c|^2$) cavity. The measured ~ 20 % contrast thus corresponds to $|t_1|^2/|t_c|^2 \simeq 0.6$ at the QD resonance (see Fig. 4 (c)). For linear polarized input, a similar division at the QD resonance results in 60% linearly polarized transmission and 20% circularly polarized transmission, from the polarization that did not match the QD spin state. This explains the $\sim$10% maximum intensity through the crossed polarizer and the higher (nearly $\sim 30\%$) contrast for the parallel polarizer. For increasing detuning between the laser and the QD transition, the cross-polarization lineshape is Lorentzian, but 1.5$\times$ wider that expected from $\gamma_\perp$, which is a sign of nonlinear QD-cavity interaction. Combining these arguments, we now find very good correspondence with the data, as shown by the red through lines in Fig. 4 (d, e).

The main purpose of this Letter is the demonstration of a polarization-degenerate QD–cavity system. An extensive study of the observed decoherence goes beyond the scope of this Letter, but we want to show first steps here. A possible mechanism behind this decoherence was found recently by Fischer et al. [20], who showed that in the quasi-2D limit of flat quantum dots an efficient hole spin – nuclear spin interaction takes place that has a strong Ising character; it only acts on spins in the QD growth direction. This decoherence mechanism is predicted to be reduced if an in-plane magnetic field is applied. We apply such a field and record the cross-polarized transmission spectra shown in Fig. 4 (f) for $B_x = 0.4$ T, and $B_x = 1$ T (g). We indeed observe a reduction of the cross-polarized transmission for linear polarized (X, Y) light. Furthermore, we see that the single resonance from Fig. 4 (e) is split by the Zeeman effect into 4 resonances, as is expected from the level diagram in Fig. 4 (b). By analyzing the energy splittings between the outermost (X) and innermost (Y) transitions and assuming $|g_e| > |g_h|$, we extract for the electron and hole in-plane g-factors $|g_e| \approx 0.4$ and $|g_h| \approx 0.1$, respectively, which is in reasonable agreement with Ref. [21]. A detailed study of the observed decoherence, for instance to distinguish between spin decoherence and spin-shelving effects (see Supplemental Material Section III), is a challenging task and will be addressed in future research.

In conclusion, we have demonstrated a polarization degenerate solid-state cavity QED system with charge control, which allows the use of arbitrary polarizations. This enabled identification of decoherence processes that are inaccessible in conventional cavities with a large polarization anisotropy. Here, simple polarimetric reflection and transmission measurements enable the study of the coherence properties of the coupled QD–cavity system, for neutral and charged quantum dots. This is an important advance for fundamental studies of spin dynamics and optical interactions in solid-state cavity QED systems, and an important step towards quantum information application such as single electron and hole spin qubits, single photon switches and quantum gates.

We would like to thank Alan Zhan for help with the sample characterization measurements. This work was supported by NSF under Grant No. 0960331 and 0901886 and FOM-NWO Grant No. 08QIP6-2.

[1] D. E. Chang, A. S. Sorensen, E. A. Demler, and M. D. Lukin, *Nat Phys*, Nature Physics **3**, 807 (2007).
[2] R. Bose, D. Sridharan, H. Kim, G. S. Solomon, and E. Waks, Physical review letters **108** (2012).
[3] V. Loo, C. Arnold, O. Gazzano, A. Lemaître, I. Sagnes, O. Krebs, P. Voisin, P. Senellart, and L. Lanco, Phys.

Rev. Lett. **109**, 166806 (2012).
[4] T. Volz, A. Reinhard, M. Winger, A. Badolato, K. J. Hennessy, E. L. Hu, and A. Imamoglu, Nat Photon **6**, 605 (2012).
[5] H. J. Kimble, Nature **453**, 1023 (2008).
[6] C. Bonato, F. Haupt, S. S. R. Oemrawsingh, J. Gudat, D. Ding, M. P. van Exter, and D. Bouwmeester, Phys. Rev. Lett. **104**, 160503 (2010).
[7] A. Dousse, J. Suffczynski, A. Beveratos, O. Krebs, A. Lemaitre, I. Sagnes, J. Bloch, P. Voisin, and P. Senellart, Nature **466**, 217 (2010).
[8] S. Reitzenstein and A. Forchel, J. Phys. D: Appl. Phys. **43**, 033001 (2010).
[9] M. T. Rakher, N. G. Stoltz, L. A. Coldren, P. M. Petroff, and D. Bouwmeester, Phys. Rev. Lett. **102**, 097403 (2009).
[10] N. G. Stoltz, M. Rakher, S. Strauf, A. Badolato, D. D. Lofgreen, P. M. Petroff, L. A. Coldren, and D. Bouwmeester, Applied Physics Letters **87**, 031105+ (2005).
[11] S. Strauf, N. G. Stoltz, M. T. Rakher, L. A. Coldren, P. M. Petroff, and D. Bouwmeester, Nature Photonics **1**, 704 (2007).
[12] A. K. Nowak, S. L. Portalupi, V. Giesz, O. Gazzano, C. Dal Savio, P. F. Braun, K. Karrai, C. Arnold, L. Lanco, I. Sagnes, A. Lemaître, and P. Senellart, Nature Communications **5** (2014), 10.1038/ncomms4240.
[13] P. M. Petroff, A. Lorke, and A. Imamoglu, Phys. Today **54**, 46 (2001).
[14] M. P. Bakker, A. V. Barve, A. Zhan, L. A. Coldren, M. P. van Exter, and D. Bouwmeester, Appl. Phys. Lett. **104**, 151109 (2014).
[15] See Supplemental Material at [URL will be inserted by publisher] for details on sample structure and characterization.
[16] P. W. Fry, I. E. Itskevich, D. J. Mowbray, M. S. Skolnick, J. J. Finley, J. A. Barker, E. P. O'Reilly, L. R. Wilson, I. A. Larkin, P. A. Maksym, M. Hopkinson, M. Al-Khafaji, J. P. R. David, A. G. Cullis, G. Hill, and J. C. Clark, Phys. Rev. Lett. **84**, 733 (2000).
[17] R. J. Warburton, C. Schaflein, D. Haft, F. Bickel, A. Lorke, K. Karrai, J. M. Garcia, W. Schoenfeld, and P. M. Petroff, Nature **405**, 926 (2000).
[18] A. Auffèves-Garnier, C. Simon, J.-M. Gérard, and J.-P. Poizat, Phys. Rev. A **75**, 053823 (2007).
[19] E. Waks and J. Vuckovic, Phys. Rev. Lett. **96**, 153601 (2006).
[20] J. Fischer, W. A. Coish, D. V. Bulaev, and D. Loss, Phys. Rev. B **78**, 155329 (2008).
[21] X. Xu, Y. Wu, B. Sun, Q. Huang, J. Cheng, D. G. Steel, A. S. Bracker, D. Gammon, C. Emary, and L. J. Sham, Phys. Rev. Lett. **99**, 097401 (2007)
.

Supplemental material: Polarization degenerate solid-state cavity QED

Morten P. Bakker,[1] Ajit V. Barve,[2] Thomas Ruytenberg,[1] Wolfgang Löffler,[1] Larry A. Coldren,[2] Dirk Bouwmeester,[1,2] and Martin P. van Exter[1]

[1] *Huygens-Kamerlingh Onnes Laboratory, Leiden University, P.O. Box 9504, 2300 RA Leiden, The Netherlands*

[2] *University of California Santa Barbara, Santa Barbara, California 93106, USA*

(Dated: October 10, 2014)

In this supplementary information we will first discuss the *sample structure and characterization* of the spatial modes. We show how the maximum Purcell factor and numerical aperture of the fundamental mode can be calculated. Then we will present a *complete description of the transmission amplitude* and will demonstrate how we estimate the scattering and absorption in the cavity region. Finally, we present *magnetic field resonant spectra* where spin-shelving is visible.

I. SAMPLE STRUCTURE AND CHARACTERIZATION

The sample under study has been grown by molecular beam epitaxy on a GaAs [100] substrate. Two distributed Bragg reflectors (DBR) surround an aperture region and a λ thick cavity region containing in the center InAs self-assembled quantum dots (QDs). The top DBR mirror consists of 26 pairs of $\lambda/4$ layers of GaAs and $Al_{0.90}Ga_{0.10}As$, while the bottom mirror consists of 13 pairs of layers of GaAs and AlAs and 16 pairs of GaAs and $Al_{0.90}Ga_{0.10}As$ layers. This way the reflectivities of top and bottom mirrors are matched in order to enable transmission and reflection measurements and optimize the incoupling efficiency. The oxidation aperture consists of a 10 nm AlAs layer embedded between 95 nm $Al_{0.83}Ga_{0.17}As$ and 66 nm $Al_{0.75}Ga_{0.25}As$ layers, providing a linearly tapered oxidation upon wet oxidation. The QDs are separated by a 20 nm tunnel barrier to n-doped GaAs and by 107 nm to p-doped GaAs.

By analyzing the confined optical modes and the wavelength splitting between the fundamental and first order optical modes, an estimation can be made of the maximum Purcell factor and the numerical aperture (NA) of the fundamental mode. A high Purcell factor is necessary to observe QD couplings close to the strong coupling regime, while the modest NA enables perfect mode-matching to external fields.

To characterize the optical properties of the confined modes, the sample is excited using an 852 nm laser diode and photoluminescence as function of position is recorded using a spectrometer. Hermite-Gaussian modes are clearly identified in Fig. 1. Following methods described in [1] we calculate the mode volume V using:

$$V = L_{cav}\frac{\lambda_{00}^3}{8\pi n_0^2\sqrt{\Delta\lambda_{01}\Delta\lambda_{10}}}, \qquad (1)$$

where $L_{eff} \approx 5\lambda/n \approx 1.4$ μm is the effective cavity length, $\lambda_{00} = 940.48$ nm is the wavelength of the fundamental mode, $n_0 \approx 3.25$ is the average refractive index,

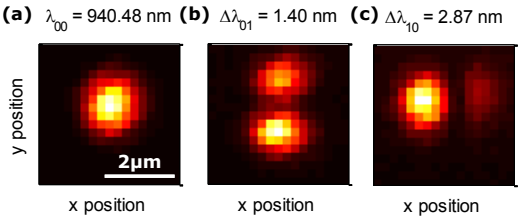

FIG. 1. Spatial PL scans of the Laguerre Gaussian modes, where (a) is the fundamental mode Ψ_{00} and (b,c) the first order Ψ_{10}/Ψ_{01} modes. Light: more PL counts. The captions denote the wavelength λ_{00} of the fundamental mode, or the wavelength splitting $\Delta\lambda_{10/01} = \lambda_{00} - \lambda_{10/01}$.

and $\Delta\lambda_{01/10}$ are the mode splittings between the $\Psi_{01/10}$ modes and the Ψ_{00} mode. By filling in the experimentally obtained values for the modepslitting we obtain $V = 2.2$ μm^3. The expected maximum Purcell factor P is given by:

$$P = \frac{3}{4\pi^2}(\frac{\lambda_{00}}{n_0})^3\frac{Q}{V}, \qquad (2)$$

where $Q = 2.6 * 10^4$ is the quality factor measured during the resonant spectroscopy scans. Using the above mentioned values we find $P = 22$. The intensity of the fundamental mode, perpendicular to the propagation direction $\hat{z}$, has the form: $I \propto \exp[-2(\frac{x^2}{w_x^2} + \frac{y^2}{w_y^2})]$, where $w_{x/y} = \frac{1}{n_0\pi}\sqrt{\frac{\lambda_{00}^3}{2\Delta\lambda_{10/01}}}$ is the mode waist. The numerical aperture of the Gaussian beam originating from the fundamental mode is given by $NA_{x/y} = \sin(\frac{\lambda_{00}}{\pi W_{x/y}})$, which gives $NA_x = 0.18$ and $NA_y = 0.25$.

II. COMPLETE DESCRIPTION OF THE TRANSMISSION AMPLITUDE

The transmission amplitude through a cavity with a coupled QD is given by [2–4]:

$$t = \eta_{out} \frac{1}{1 - i\Delta + \frac{2C}{1 - i\Delta'}}, \tag{3}$$

where the parameters are defined in the main text. We will here quantify the role of losses and its effect on the out-coupling efficiency $\eta_{out} = \frac{2\kappa_m}{\kappa}$, defined as the probability that a photon in the mode will leave the cavity through the top or bottom mirror. Here κ_m is the damping rate of each Bragg mirror, κ_s is the scattering and absorption rate inside the cavity, and $\kappa = 2\kappa_m + \kappa_s$ is the total cavity intensity damping rate. Furthermore $\kappa_m = T_{mirror}/t_{round}$, where T_{mirror} is the transmittivity of a single mirror and $t_{round} = 2nL_{cav}/c$ is the cavity round trip time. n is the average refractive index, $L_{cav} \approx 5\lambda/n$ the effective cavity length, c is the speed of light and $\lambda \approx 940$ nm the wavelength in vacuum.

The mirror damping rate $\kappa_m \approx 11$ ns^{-1} is calculated from the sample design parameters. Three observations consistently yield $\kappa_s \approx 55$ ns^{-1}: (i) the measured quality factor $Q \approx 2.6 \times 10^4$ is lower than $Q = 9.1 \times 10^4$ as determined by the mirror transmittivity $T_{mirror} = 3.4 * 10^{-4}$ and cavity length, and corresponds to $\kappa = 77$ ns^{-1}, (ii) the minimum reflectivity of the empty cavity $\frac{R_{min}}{R_{max}} \approx 0.5$, and (iii) the maximum transmission $T \approx 0.08$, (including a $\sim 30\%$ reflectivity at the GaAs to air interface at the back of the sample). We attribute this scattering rate κ_s to (spectrally broad) absorption losses in the doped layers and scattering by the oxide aperture. Reducing κ_s, for example by using a lower doping concentration, is a major concern in future sample designs.

Finally we will comment on the case of non-perfect mode matching. The total transmission T through the cavity is then given by $T = \eta_{in}\eta_T|t|^2$, where η_{in} is the in-coupling efficiency and η_T is the collection efficiency at the transmission port. The total reflection is given by $R = \eta_R|1 - \eta_{in}t|^2$, where η_R is the collection efficiency at the reflection port. In case of perfect mode matching $\eta_{in} = \eta_R = \eta_T = 1$.

III. MAGNETIC FIELD RESONANT SPECTRA

Resonant reflection and transmission spectra are presented for $B_x = 1$ T in Fig. 2. Light is polarized linearly parallel (X) or perpendicular (Y) to the magnetic field direction. Due to spin-shelving effects the QD features (black arrows) are hardly visible anymore.

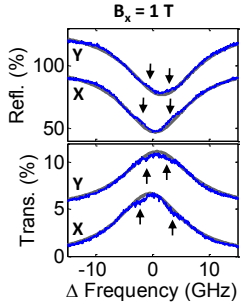

FIG. 2. Resonant reflection and transmission spectra for an in-plane magnetic field of $B_x = 1$ T. An offset between the different curves is added. The QD features are marked by the black arrows.

[1] C. Bonato, J. Gudat, K. de Vries, S. M. Thon, H. Kim, P. M. Petroff, M. P. van Exter, and D. Bouwmeester, Opt. Lett. **37**, 4678 (2012).
[2] V. Loo, C. Arnold, O. Gazzano, A. Lemaître, I. Sagnes, O. Krebs, P. Voisin, P. Senellart, and L. Lanco, Phys. Rev. Lett. **109**, 166806 (2012).
[3] A. Auffèves-Garnier, C. Simon, J.-M. Gérard, and J.-P. Poizat, Phys. Rev. A **75**, 053823 (2007).
[4] E. Waks and J. Vuckovic, Phys. Rev. Lett. **96**, 153601 (2006)
.

References

[1] Y. Makhlin, G. Schön, and A. Shnirman, *Quantum-state engineering with Josephson-junction devices*, Rev. Mod. Phys. **73**, 357 (2001).

[2] M. Saffman, T. G. Walker, and K. Mølmer, *Quantum information with Rydberg atoms*, Rev. Mod. Phys. **82**, 2313 (2010).

[3] W. Pfaff, B. J. Hensen, H. Bernien, S. B. van Dam, M. S. Blok, T. H. Taminiau, M. J. Tiggelman, R. N. Schouten, M. Markham, D. J. Twitchen, and R. Hanson, *Unconditional quantum teleportation between distant solid-state quantum bits*, Science **345**, 532 (2014).

[4] J. J. Pla, K. Y. Tan, J. P. Dehollain, W. H. Lim, J. J. Morton, D. N. Jamieson, A. S. Dzurak, and A. Morello, *A single-atom electron spin qubit in silicon*, Nature **489**, 541 (2012).

[5] A. Imamoglu, D. D. Awschalom, G. Burkard, D. P. DiVincenzo, D. Loss, M. Sherwin, and A. Small, *Quantum Information Processing Using Quantum Dot Spins and Cavity QED*, Phys. Rev. Lett. **83**, 4204 (1999).

[6] H. J. Kimble, *The quantum internet*, Nature **453**, 1023 (2008).

[7] T. Volz, A. Reinhard, M. Winger, A. Badolato, K. J. Hennessy, E. L. Hu, and A. Imamoglu, *Ultrafast all-optical switching by single photons*, Nat Photon **6**, 605 (2012).

[8] C. S. Munoz, E. del Valle, A. G. Tudela, MullerK., LichtmanneckerS., KaniberM., TejedorC., FinleyJ. J., and LaussyF. P., *Emitters of N-photon bundles*, Nat Photon **8**, 550 (2014).

[9] A. Rundquist, M. Bajcsy, A. Majumdar, T. Sarmiento, K. Fischer, K. G. Lagoudakis, S. Buckley, A. Y. Piggott, and J. Vučković, *Nonclassical higher-order photon correlations with a quantum dot strongly coupled to a photonic-crystal nanocavity*, Phys. Rev. A **90**, 023846 (2014).

[10] E. Waks and J. Vuckovic, *Dipole Induced Transparency in Drop-Filter Cavity-Waveguide Systems*, Phys. Rev. Lett. **96**, 153601 (2006).

[11] D. Walls and G. Milburn, *Quantum Optics*, Springer, 1994.

[12] V. Loo, C. Arnold, O. Gazzano, A. Lemaître, I. Sagnes, O. Krebs, P. Voisin, P. Senellart, and L. Lanco, *Optical Nonlinearity for Few-Photon Pulses on a Quantum Dot-Pillar Cavity Device*, Phys. Rev. Lett. **109**, 166806 (2012).

[13] M. Bayer, G. Ortner, O. Stern, A. Kuther, A. A. Gorbunov, A. Forchel, P. Hawrylak, S. Fafard, K. Hinzer, T. L. Reinecke, S. N. Walck, J. P. Reithmaier, F. Klopf, and F. Schäfer, *Fine structure of neutral and charged excitons in self-assembled In(Ga)As/(Al)GaAs quantum dots*, Phys. Rev. B **65**, 195315 (2002).

[14] J. Gudat, *Cavity Quantum Electrodynamics with Quantum Dots in Microcavities*, PhD thesis, Leiden University, 2012.

[15] M. P. Bakker, A. V. Barve, A. Zhan, L. A. Coldren, M. P. van Exter, and D. Bouwmeester, *Polarization degenerate micropillars fabricated by designing elliptical oxide apertures*, Applied Physics Letters **104** (2014).

[16] P. Kaer, T. R. Nielsen, P. Lodahl, A.-P. Jauho, and J. Mørk, *Microscopic theory of phonon-induced effects on semiconductor quantum dot decay dynamics in cavity QED*, Phys. Rev. B **86**, 085302 (2012).

[17] J. Houel, A. V. Kuhlmann, L. Greuter, F. Xue, M. Poggio, B. D. Gerardot, P. A. Dalgarno, A. Badolato, P. M. Petroff, A. Ludwig, D. Reuter, A. D. Wieck, and R. J. Warburton, *Probing Single-Charge Fluctuations at a* GaAs/AlAs *Interface Using Laser Spectroscopy on a Nearby InGaAs Quantum Dot*, Phys. Rev. Lett. **108**, 107401 (2012).

[18] B. Urbaszek, X. Marie, T. Amand, O. Krebs, P. Voisin, P. Maletinsky, A. Högele, and A. Imamoglu, *Nuclear spin physics in quantum dots: An optical investigation*, Rev. Mod. Phys. **85**, 79 (2013).

[19] C. Latta, A. Hogele, Y. Zhao, A. N. Vamivakas, P. Maletinsky, M. Kroner, J. Dreiser, I. Carusotto, A. Badolato, D. Schuh, W. Wegscheider, M. Atature, and A. Imamoglu, *Confluence of resonant laser excitation and bidirectional quantum-dot nuclear-spin polarization*, Nat Phys **5**, 758 (2009).